AIAA JOURNAL
Vol. 62, No. 12, December 2024

Direct Numerical Simulation of Tandem-Wing Aerodynamic Interactions at Low Reynolds Number

Chenchen Zhao,* Duo Wang,† Ting Yu,† and Hongyi Xu‡
Fudan University, 200433 Shanghai, People's Republic of China

https://doi.org/10.2514/1.J064345

A three-dimensional direct numerical simulation was conducted to investigate the vortex–wing interactions through two NACA 0012 stationary wings placed in tandem at a low Reynolds number $Re = 10{,}000$. The aerodynamic characteristics and three-dimensional flow structures were analyzed for the tandem wings. The back wing disturbed by the upstream vortices gained an evident increase in aerodynamic performance, where the advantage is related to the suppression of the large-scale vortex formation near the trailing edge. The Liutex method was applied to visualize the vortical structures for investigating the three-dimensional evolution and instability when interacting with the back wing. The upstream wake triggered dual-secondary vortices and intensified the secondary instability on the back wing. The induced vortices contributed to the lift enhancement because they provided an extra low-pressure region when propagating downstream on the suction side of the back wing. Because of the three-dimensional destabilization, the vortex interaction in the evolution process accelerated the transition and injection of the high-momentum flow into the boundary layer attached to the back wing, energizing the turbulent boundary layer and eliminating the large-scale separation near the trailing edge. This study provided a new perspective on the enhanced aerodynamic performance of tandem layout.

Nomenclature

A	=	amplitude
C_D	=	drag coefficient
C_{DF}	=	friction drag coefficient
C_{DP}	=	pressure drag coefficient
C_L	=	lift coefficient
C_p	=	pressure coefficient
c	=	chord length
f	=	frequency
k	=	wave number
L_z	=	spanwise length
$\boldsymbol{R}$	=	Liutex vector
R_x	=	streamwise component of Liutex vector
R_z	=	spanwise component of Liutex vector
Re	=	Reynolds number based on chord length, $u_\infty c/\nu$
$\boldsymbol{S}$	=	shear vector
Sr	=	Strouhal number based on chord length, fc/u_∞
T	=	period, $1/f$
u_∞	=	freestream velocity
α	=	angle of attack
λ	=	wavelength
ν	=	kinematic viscosity
ω	=	vorticity

I. Introduction

WINGS in a tandem arrangement, inspired by bird formation flight in nature, are attractive to the aerospace engineering community owing to their aerodynamic performance, superior stability, and even energy harvesting. Similar configurations are widely observed in diverse scenarios, such as canard wing aircraft, flight refueling, turbomachinery blades, and bird formation flight [1]. It is worth noticing that the flow past the wings lined up differs from the case of an isolated configuration, in which the particular interest for a tandem layout is that the back wing can interact with the upstream wake, where the aerodynamics become, in general, complicated and turbulent. The vortical structures, shed from the front wing and thereafter interacting with the back wing, are the critical attributions to the aerodynamic benefits between two closely located wings [2]. The presence of additional disturbances introduced by the incoming vortical structures may be a dominant factor governing the flowfield and interfering with the aerodynamic performance of the downstream body.

Several previous studies have demonstrated the effects of tandem-wing configuration in terms of better aerodynamic performance and efficiency [3,4]. These studies have consistently demonstrated a significant reduction in drag and an increase in the lift-to-drag ratio over a wide range of flight conditions compared with the monoplane case. Similarly, investigations into the tandem configuration under pitching/heaving motions have been conducted for better aerodynamic force production and propulsive efficiency [5,6]. This favorable choice is commonly observed in the bird flock flight and fish school navigation for saving energy and enhancing efficiency [7,8]. Further, most existing studies have primarily focused on the aerodynamic performance variations in different spatially geometric arrangements among the adjacent airfoils, such as streamwise gaps and transverse offset distances, under the conditions of various angles of attack. The effects on the flowfield and forces in moving wing spacings were investigated by Broering and Lian [9] for a low Reynolds number, where the optimal spacing for the maximum lift of tandem wings was claimed to be at one wing chord length. A parametric study on the effects of various geometric parameters was carried out to investigate the aerodynamic characteristics of a fixed tandem-wing vehicle configuration in low-Reynolds-number regimes [10–13]. Jones et al. [14] reported that the aerodynamic efficiency was improved in the case of post-stall angles of attack while being degraded at the small incident angles at a larger Reynolds number. These studies might be designed to obtain the optimal arrangement of the tandem configuration to maximize the aerodynamic performance rather than providing a detailed explanation of the underlying mechanisms of the performance changes, especially the quantitative role of the upstream vortical structures in the downstream interactions and aerodynamic performance.

In the tandem configuration, the flow structures from the upstream body play a vital role in aerodynamic interactions because the downstream object resides in the wake of the front wing [15]. Rockwell [16] reviewed the flow physics of the interactions between vortices and downstream bodies, in which the distortion of the incident vortex

Received 30 April 2024; revision received 2 July 2024; accepted for publication 3 July 2024; published online 30 August 2024.

*Ph.D. Candidate, Department of Aeronautics and Astronautics.
†Postdoctoral Researcher, Department of Aeronautics and Astronautics.
‡Professor, Department of Aeronautics and Astronautics; hongyi_xu@fudan.edu.cn (Corresponding Author).

was considered based on the distributed vorticity. The interaction patterns were therefore classified into three basic categories according to the orientation of the incident vortex interacting with the leading edge of the downstream body: parallel vortex, streamwise vortex, and normal vortex interactions. The proposed classification simplified the studies toward understanding the mechanisms and characteristics of generic vortex–body interactions. As one of the most fundamental classes, parallel vortex–body interaction has been studied for years on the details of vortex distortion and its consequent unsteady loading on the wall surface. Specifically, one practical scenario was studied by Gursul and Rockwell [17], in which the von Kármán vortex street of an upstream bluff body interacts with a downstream body with an elliptical edge. The wavelength and circulation of the incident vortex street were found to be dominated by the vortex distortion and severity of the interaction. Lua et al. [18] found that the correlation between transient thrust and wing–wake interactions depended on structures from the front wing that the back wing confronts. In addition, numerical analyses of clockwise and counterclockwise parallel vortical–airfoil interactions have been conducted in recent studies [19,20]. The vortex structures were claimed to propagate downstream as a dipole, inducing a pressure disturbance and changing the lift when departing from the trailing edge.

However, most studies on parallel vortex interactions were traditionally assumed to be two-dimensional (2-D) with a lack of in-depth explanation. Little attention has been paid to the impact of three-dimensionality and spanwise scales of the vortical structure in the vortex–wing interaction. Many studies have reported that three-dimensional (3-D) characteristics and spanwise instability could be found in various configurations. Hayakawa and Hussain [21] confirmed that the coherent structures in the nominally 2-D wake of a cylinder exhibited evident 3-D characteristics. Gupta et al. [22] elucidated the effects of angles of attack and Reynolds numbers on the development of three-dimensionality with different 3-D instability modes in a NACA 0012 airfoil wake at low Reynolds numbers. Son et al. [23] observed different spanwise instabilities and deformations in both oscillating airfoils and wings. Evidence suggests that alterations in the magnitude of the vorticity component in different directions would impact the correlation of the instantaneous loadings and hence the time-averaged aerodynamic forces on the body [16]. Therefore, the spanwise scale of the incident coherent structures ought to be accounted for in the investigation because these structures would tangibly affect the downstream flowfield and interact with the downstream body.

In the existing studies on the airfoil–vortex interaction (AVI), it was a common practice that an isolated vortex or vortex street was generated by a bluff body to interact with the downstream airfoil [19,20,24,25]. In contrast, the responses on the vortical structures in an airfoil wake interacting with a downstream body are barely mentioned. It was found that the airfoil wakes at a post-stall attack angle were considered to behave similarly to the vortical structures of a bluff body, which has been intensively discussed for decades [26]. However, at lower angles of attack, the airfoil wake demonstrated quite different characteristics, even when flow separation occurred without a reattachment [27]. Another concern is that when operating at a lower Reynolds number, the flow over airfoils is subject to several challenges, such as laminar separation, transition, and turbulent reattachment. Direct numerical simulation (DNS) is expected to be an effective approach for addressing the complex physics in the multiple-wing interactions at low Reynolds numbers.

In this study, the resolution of the flow features in the tandem-wing layout at a low Reynolds number was attempted using the high-fidelity DNS method, where particular attention was focused on the vortical structure evolution and aerodynamic interactions. Based on the preliminary results of the 2-D tandem-airfoil case [28], this study further extended the simulation to 3-D wing sections at a fixed low angle of attack and low Reynolds number. The flow developed into a state of unsteady wake due to the primary instability in the 2-D case, and then the data were applied as the initial condition in the 3-D simulation until the flow was fully developed. To the best of the authors' knowledge, very few studies have reported low-Reynolds-number flow over tandem wings targeted at thoroughly resolving vortical structures and aerodynamic interaction mechanisms.

As the crucial research objects in the flow, the vortical structures play a vital role in the aerodynamic interactions between the front and back wings. However, the vortex identification (VI) method remains one of the fundamentally challenging issues in the fluid dynamics community. Traditional identification methods, such as vorticity ω and many other VI quantities [29–32] of Q and λ_{ci}, have been widely used in previous analyses. Until recently, a state-of-the-art VI method was proposed by Liu et al. and Gao and Liu [33,34] based on the Liutex vector quantity $\boldsymbol{R}$. The Liutex vector was found to better distinguish the rotating motion from the shearing motion in vortex representation due to the Liutex–shear ($\boldsymbol{R}$–$\boldsymbol{S}$) decomposition of the vorticity vector ω. It claims that the Liutex vector contains the key elements of the vortex in terms of its vector direction, representing the local rotating axis and its magnitude standing for twice the angular speed of the local rigid rotation. This new VI method provides more precise observations of the vortex evolutions to interrogate the vortex–wing interactions in this study.

This study was motivated by the necessity for further insight into the aerodynamic mechanisms in the role coherent structures play in the tandem-wing interactions for the low-Reynolds-number flow. The aerodynamic performance of the back wing was found to be closely related to the vortices shed from the front wing, and the vortices interacted with the back wing in the form of upper and lower layers of vortices with their distinctive evolution patterns. In the following sections, the detailed model configuration and numerical simulation methodology for the present DNS are briefly discussed. The analyses and discussions are subsequently elaborated, including the aerodynamic performance and their closely related coherent structure evolution characteristics. Furthermore, concluding remarks and important results are summarized, which provide an in-depth understanding of the wing–vortex interaction phenomena.

II. Methodology

A. Numerical Methods

For the flow around the wings in tandem, as illustrated in Fig. 1, the governing equations were the 3-D incompressible Navier–Stokes (N–S) equations written in nondimensional form as

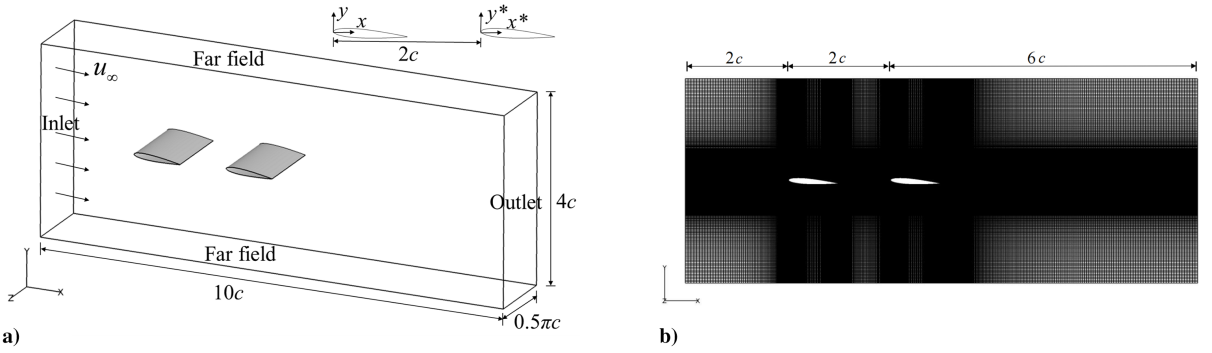

Fig. 1 Simulation setups: a) computational domain and boundary conditions; b) mesh settings in the x-y plane of the computational configuration.

$$\nabla \cdot \boldsymbol{U} = 0 \tag{1}$$

$$\frac{\partial \boldsymbol{U}}{\partial t^*} + (\boldsymbol{U} \cdot \nabla)\boldsymbol{U} = -\nabla P + \frac{1}{Re}\nabla^2 \boldsymbol{U} \tag{2}$$

where $\boldsymbol{U}$ ($\equiv \boldsymbol{u}/\boldsymbol{u}_\infty$) is the nondimensional velocity vector, P ($\equiv p/\rho u_\infty^2$) is the nondimensional pressure, and the nondimensional time t^* is given as $t^* = tu_\infty/c$. Here, $\boldsymbol{u}$ is the velocity, p is the pressure, and ρ is the density. All variables in the equations were normalized by the freestream velocity u_∞ and the chord length of the wing c. The nondimensional parameter Reynolds number Re is defined as $Re = u_\infty c/\nu$, where ν is the kinematic viscosity.

The governing equations were tackled by DNS using an in-house incompressible flow solver in a 3-D space. The solver was previously validated for turbulence in a square annular duct [35]. More recently, this solver was applied to investigate the instability around cylinders [36]. The incompressible equations were decoupled using the fractional step method with a predictor–corrector procedure proposed by Kim and Moin [37]. The spatial discretization method in the solver was based on the finite volume method, in which the dependent variables $\boldsymbol{U}$ and P were allocated to staggered grids. In spatial discretization, the convection term was discretized using the total variation diminishing-type scheme, and the second-order center difference was applied to the diffusion term and pressure gradient. Temporal discretization was performed using the second-order Adams–Bashforth explicit scheme and the second-order Adams–Moulton implicit scheme for the convection and diffusion terms, respectively. Time stepping in the simulation was conducted with a constant time step of $\Delta t = 1.0 \times 10^{-4}$, conforming to the stability criterion with the maximum Courant–Friedrichs–Lewy number being less than 1.0. The pressure Poisson equation was then solved using the flexible cycle additive correction multigrid technique [35] to ensure solution accuracy and accelerate convergence. The inner wall boundary of the wing was handled using the ghost-cell immersed boundary method [38,39], which is capable of handling the wing geometry without the necessity of imposing an additional force. For the 3-D configuration, an infinite span was assumed in this study, and periodic boundary conditions were prescribed in the spanwise direction, which facilitates accurate and efficient resolution of the pressure Poisson equation through the fast Fourier spectral approach.

B. Simulation Setup

The computational domain and boundary conditions for the flow around tandem wings are illustrated in Fig. 1. Two identical NACA 0012 wings at $\alpha = 4$ deg with an infinite span placed in a horizontal tandem arrangement were immersed in a uniform freestream from the inlet. The wings were rescaled to the unit chord length c with sharp trailing edges. The domain sizes were set as $10c$ in the streamwise direction and $4c$ in the transverse direction, which were confirmed to be sufficient for the simulation [40]. The streamwise gap between the leading edges of the two wings was given at $2c$, and the offset distance was chosen at 0. The leading edges of the two wings were placed in the x-y plane at the locations of $(x, y) = (0, 0)$ and $(x^*, y^*) = (2c, 0)$, respectively. The inlet and far-field boundaries were at $2c$ upstream for the front wing, whereas the outlet side was at $6c$ downstream from the leading edge of the back wing. The spanwise scale in the existing simulations was usually set at a length smaller than c, with $0.8c$ being widely accepted as the sufficient length for a massively separated flow [40]. Because of the low-Reynolds-number factor in this simulation, the spanwise length was set at $L_z = 0.5\pi c$, aimed at well resolving the turbulent structures and their spanwise scales.

Appropriate boundary conditions were essential for the simulation, as shown in Fig. 1a. The uniform incoming flow $\boldsymbol{u} = (u_\infty, 0, 0)$ with no disturbance was imposed on the domain inlet. The outlet boundary at the domain far streamwise end was prescribed as the zero derivative of each velocity component derivative, $\partial \boldsymbol{u}/\partial x = 0$, equivalent to a Neumann-type condition. Further, the top and bottom sides of the domain were set as the far-slip conditions ($\partial u/\partial y = 0$, $v = 0$, and $\partial w/\partial y = 0$), and the no-slip boundary condition for velocity was applied to the wing wall surfaces ($\boldsymbol{u} = \boldsymbol{0}$). The periodic boundary condition was imposed to represent the infinite wing length in the spanwise direction.

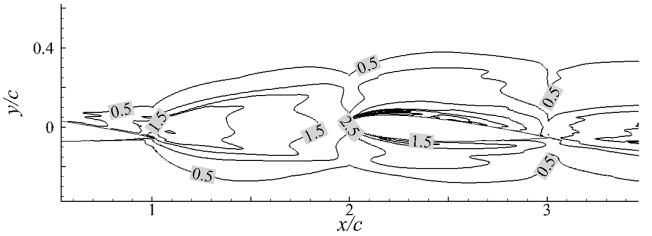

Fig. 2 Ratio of h/η between the local mesh size and Kolmogorov length scale near the back wing at the midspan location.

Regarding the grid resolution requirements in the DNS, the refined meshes were demanding for the multiple-scale nature of the flow, as represented by the temporal and spatial spectra in the turbulence analyses. On the x-y plane, the grid was clustered around the wing surface and wake region. The resolutions near the solid boundary were identical for both the front and back wings. The mesh density presented an increased resolution toward the wing surfaces and wake region, as shown in Fig. 1b. For the 3-D simulation, the structured Cartesian mesh shown in Fig. 1b was extruded equally spaced in the spanwise direction, generating hexahedrons throughout the entire domain.

For quality simulation, sufficient spatial resolution as a crucial factor should be targeted at resolving the smallest coherent structures in the flow. Given that the current wing flow was considered at a low Reynolds flow, the Kolmogorov length scale η, which commonly represents the minimum scale in a flow, was calculated to examine the grid resolution. According to Moin and Mahesh [41], the spatial resolution scale h of a grid has to be at the order of Kolmogorov scale $O(\eta)$, where the local mesh size h and Kolmogorov length scale η are defined as

$$h = (\Delta x \Delta y \Delta z)^{1/3}; \qquad \eta = (\nu^3/\epsilon)^{1/4} \tag{3}$$

where $\epsilon = 2\nu\overline{s_{ij}s_{ij}}$ is the turbulent kinetic energy (TKE) dissipation rate, and s_{ij} are the components of the fluctuating strain rate tensor $\boldsymbol{s} = 1/2(\nabla \boldsymbol{u}' + (\nabla \boldsymbol{u}')^T)$.

A necessary posterior analysis was performed to assess the resolution ratio distribution h/η. Because the mesh was equally spaced in the spanwise direction, the ratio distribution h/η at a typical midspan location is presented in Fig. 2. The distribution of h/η near the back wing shows that the local mesh size was at most two to three times that of the Kolmogorov length scale η, and the ratios in most of the domain were approximately and even less than 1. Considering the analysis and previous experience gained from the 2-D case, the mesh in the current study was deemed sufficient to achieve a quality simulation resolution and to resolve the coherent scales of interest at a lower Reynolds number.

III. Results and Analyses

A. Time-Averaged Flowfields

The aerodynamic forces acting on the wings were defined by integrating the pressure p and shear stress τ over the entire wall surface of each wing section ∂W:

$$\boldsymbol{F} = \oint_{\partial W} (\tau \boldsymbol{n} - p\boldsymbol{n})\, \mathrm{d}s \tag{4}$$

The drag C_D and lift C_L coefficients are generally used to characterize the aerodynamic forces defined by

$$C_D = \frac{F_x}{(1/2)\rho u_\infty^2 c L_z}; \qquad C_L = \frac{F_y}{(1/2)\rho u_\infty^2 c L_z} \tag{5}$$

Table 1 Quantitative evaluation of the aerodynamic performance of the NACA 0012 wing at $Re = 10^4$ and $\alpha = 4$ deg

Case	Method	$\overline{C}_L$	$C_{L,\mathrm{RMS}}$	$\overline{C}_D$	$\overline{C}_{\mathrm{DP}}$	$\overline{C}_{\mathrm{DF}}$	$\overline{C}_L/\overline{C}_D$
Front wing	3-D DNS	0.171	0.181	0.044	0.030	0.014	3.89
Back wing	3-D DNS	0.190	0.235	0.027	0.016	0.011	7.03
Front airfoil [28]	2-D DNS	0.185	— —	0.052	0.030	0.022	3.56
Back airfoil [28]	2-D DNS	0.206	— —	0.043	0.024	0.019	4.79
Isolated wing [42]	3-D ILES	0.165	— —	0.046	— —	— —	3.59
Isolated wing [43]	Experiment	0.170	— —	— —	— —	— —	— —

where F_x and F_y are the aerodynamic forces in the streamwise and transverse directions, respectively; c and L_z represent the chord length and spanwise length of the wing, respectively. The contributions of pressure and viscous stress for the drag are given as pressure drag C_{DP} and friction drag C_{DF}, respectively. The statistical aerodynamic parameters (in which the superscript $\overline{\square}$ indicates time averaging) listed in Table 1 were obtained from the 50 nondimensional time units where the record starts at $t^* = 0$ when the instantaneous flow is fully developed. The performance of the front wing in the current tandem configuration agrees well with the results of an isolated NACA 0012 obtained by 3-D implicit large-eddy simulation (ILES) [42] and experiments [43] at the same attack angle and Reynolds number. Because of the unique downstream location compared with the front base geometry, the back wing exhibited a distinctive performance, with the time-averaged lift coefficient $\overline{C}_L$ and drag coefficient $\overline{C}_D$ being 0.19 and 0.027, respectively, which shows approximately 12% increase in lift and 39% decrease in total drag. Therefore, the back wing gained an aerodynamic advantage over the front wing, with approximately 80% of the time-averaged net effect increase in $\overline{C}_L/\overline{C}_D$. Figure 3 [44] summarized the airfoil lift-to-drag ratio ranges from low Reynolds-number scales to high Reynolds-number regimes. The Reynolds number in the current tandem configuration is close to the insects and micro air vehicles (MAVs). The lift-to-drag ratio of the front wing was in accordance with the range of smooth conventional airfoils at low Reynolds numbers, whereas the ratio of the back wing was above the range with an apparent performance improvement, as evident from the marks in Fig. 3. The back wing was subjected to an increase in the lift coefficient and a decrease in the pressure and friction drag, and this trend was consistent with the precursory 2-D airfoil simulation [28]. The time-averaged enhancement effect is analogous to the aerodynamic benefits induced by the upstream bluff body in downstream geometry [25,45,46].

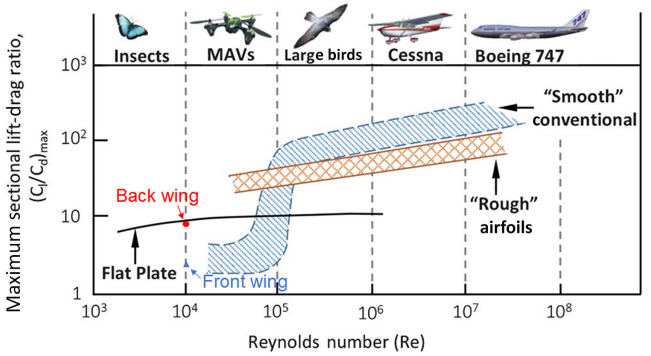

Fig. 3 Ranges of the lift-to-drag ratio at various Reynolds numbers on airfoils [44] marked with the results of the tandem wings.

For the flow over wings at a small angle of attack and low Reynolds number, pressure usually contributes most of the drag forces [47]. Based on the results in Table 1, the pressure drag accounted for approximately 68 and 60% of the total drag for the front and back wings, respectively, and friction was responsible for approximately the remaining 32 and 40%. Given the total drag decline for the back wing, the primary contributions were also from the pressure drag, whereas the change in viscous drag was comparatively minor. Anyoji et al. [48] found that the pressure drag is the dominant part for airfoils whose gap between airfoils is considerably more significant than that in the viscous drag at low Reynolds numbers. Therefore, the overall aerodynamic performance improvement for the back wing was mainly attributed to the changes in lift and pressure drag.

Because of the noticeable impact on the lift and pressure drag, the pressure coefficient C_p on the wing surface is crucial for determining the aerodynamic performance of the wing and reflecting the interactions between the wings. The time-averaged distributions of $\overline{C}_p$ are illustrated in Fig. 4 for the two wings in tandem. A noticeable feature is that the back wing exhibited a lower suction peak and pressure peak than the front wing, whereas a pronounced low-pressure region was visible near the trailing edge of the front wing. However, weakened and mild pressure gradients near the leading edge occurred on both the upper and lower surfaces of the back wing, which led to increased pressure differences between the suction and pressure surfaces for a larger portion of the back wing. The increase in the lift coefficient and decrease in the pressure drag coefficient were attributed to these factors, which boosted the aerodynamic performance from the surface pressure differences between the two wings.

The mean flowfields around the tandem wings are illustrated in Fig. 5 in terms of the time- and spanwise-averaged streamwise velocities and streamlines, which show noticeable differences in the reversed flow pattern near the trailing edge between the front and back wings. An elongated and bounded recirculation zone protruding quite beyond the trailing edge dominated the flow separation on the front wing, as shown in Fig. 5a. A counter-rotating

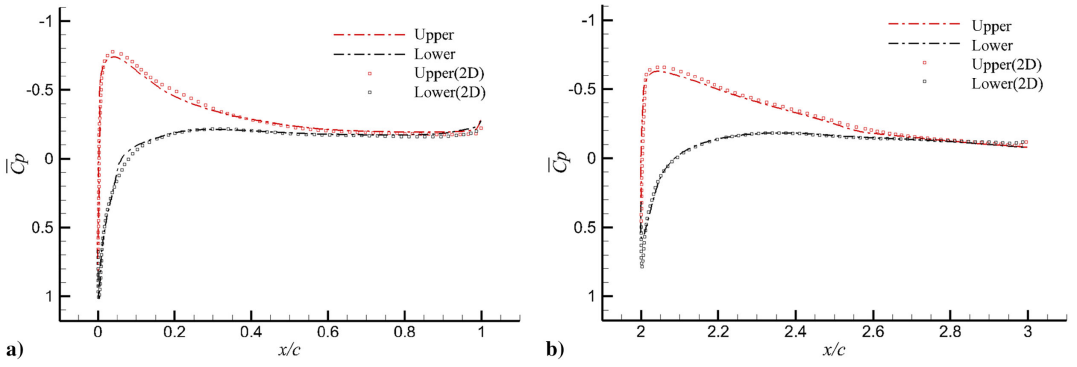

Fig. 4 Time- and spanwise-averaged pressure coefficient distributions on the wing surfaces for the a) front wing and b) back wing overlapped by the 2-D tandem airfoil case [28].

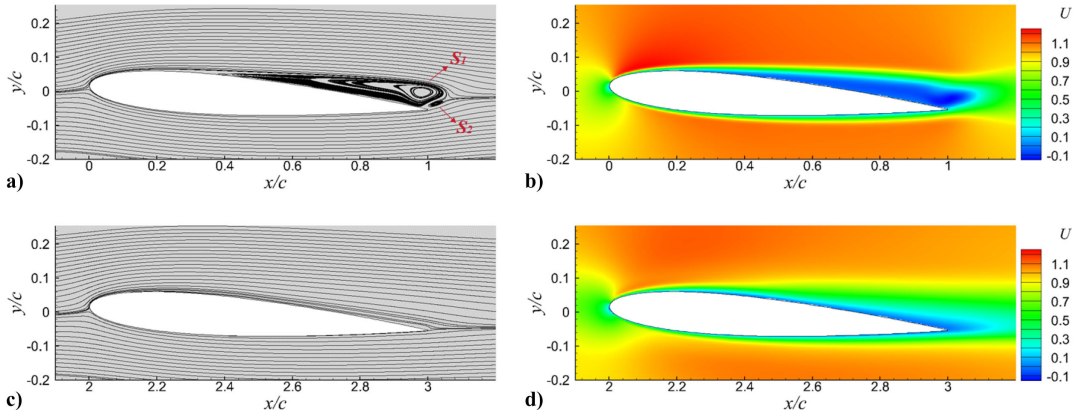

Fig. 5 Time- and spanwise-averaged streamlines for the a) front wing and c) back wing; isocontours of the mean streamwise velocity for the b) front wing and d) back wing.

vortex S_2, as the secondary structure originating from the trailing edge, was found to pair with the dominant clockwise structure S_1 in the recirculation zones. Similar structures were reported by Tank et al. [49] for the time-averaged flowfield of a cambered airfoil below the critical angle of attack. For the front wing, the trailing-edge separation bubble started approximately from the streamwise location of $x/c = 0.4$ to $x/c = 1.1$, where the separation point coincided with that of an isolated airfoil at the same attack angle and Reynolds number [42]. Accordingly, a long belt zone of negative streamwise velocity was observed near the trailing edge, as shown in Fig. 5b. Large-scale vortex formation is likely to emerge in the trailing-edge separation bubble area in the instantaneous flow, where this area is associated with the time-averaged low-pressure region on the trailing edge, as shown in Fig. 4a. Contrary to the pronounced separation on the front wing, the mean streamlines passing over the back wing were tightly attached to the wing surface nearly without any sign of flow separation and large-scale structure formation, as shown in Fig. 5c. The velocity contour near the back wing in Fig. 5d confirms that the negative streamwise velocity zone was significantly suppressed and restricted closer to the wall surface and was more streamlined toward the trailing edge on the suction side. These distinctive streamwise velocity patterns on the wings in tandem provide evidence that the flow separation suppression tends to weaken the vortical structure formation on the back wing and provides an aerodynamic advantage over the front wing.

The flow separation topology between the two wings was further investigated from a more detailed 3-D perspective by demonstrating the mean flow recirculation areas where the time-averaged streamwise velocity became negative, as depicted by the isosurfaces of $u/u_\infty = -0.001$ (Fig. 6). A more prominent and nearly 2-D recirculation region was identified as the laminar separation phenomenon on the front wing. The top view exhibits the 3-D feature of the wavy boundaries of these separation bubbles near $x/c = 1.05$ along the wingspan, which was identified in the wake region beyond the trailing edge of the front wing. This spanwise wavy feature shown in the isosurface topology implies that the secondary instability transition started in the front-wing wake region at a prominent spanwise wavelength at approximately $\lambda_z = \lambda/L_z = 0.125$. However, regarding the back wing, recirculation occurred further downstream, and it evolved into many isolated bubbles in streak patterns scattered along the span of the trailing area on the suction surface. The 3-D scattered separation bubbles distributed along the span were characterized by a spanwise wavelength nearly $\lambda_z = 0.125$, equal to that in the front-wing wake. The spanwise spacing distribution may be related to the upstream wake disturbance. The upstream wake generated by the front wing effectively suppressed and delayed separation on the back wing, which eliminated the formation of large-scale recirculation or separation bubbles. This phenomenon is consistent with a previous study [50], where it was claimed that appropriate excitation overcame the adverse pressure gradient and suppressed the separation region. Instead, the separated bubbles on the back wing show a highly 3-D character and evident streamwise structure, which explains that intensified secondary instability and 3-D vortex evolution occurred in the back wing due to the upstream flow interference from the front wing.

The investigations of the mean flowfield suggest that the superior performance of the back wing in the lift and drag is attributed to the wake interference induced by the upstream wing, which significantly suppresses the large separation bubble and breaks into scattered and isolated 3-D separation zones. This discovery is similar to that observed in a wing placed in the wake of a bluff

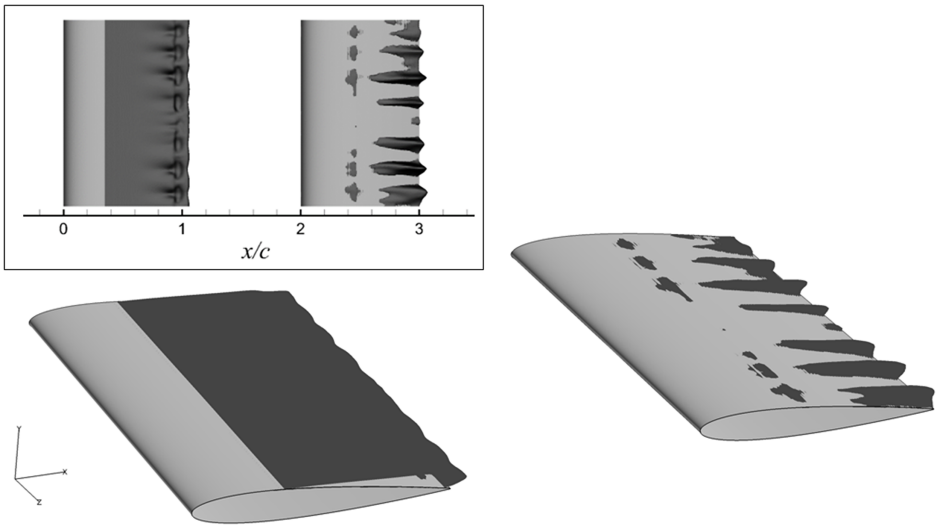

Fig. 6 Time-averaged recirculation regions for the tandem wings visualized by the isosurface of $u/u_\infty = -0.001$, with the top view in the inset.

body by Zhang et al. [1], who concluded that the increase in lift was due to delayed flow separation and subsequent reattachment. The current study found that even at a much lower Reynolds number without flow reattachment, the wake from a streamlined body can also positively impact the downstream body to resist flow separation and enhance aerodynamic performance.

B. Transient Behaviors

Considering the aerodynamic performance improvement for the back wing, the impacts of upstream disturbances on the back wing are not only reflected by the time-averaged behaviors but are also more interested in the transient responses of the downstream body. This study attempted to comprehensively look into these detailed transient behaviors and aerodynamic responses of the related vortex–wing interactions for the tandem wings.

The time-dependent lift and drag coefficients of the tandem wings are plotted in Fig. 7 over the selected 15 nondimensional time units superimposed by the preliminary 2-D results [28]. The time-dependent C_L exhibited periodic oscillations, similar to the 2-D case. A noticeable feature of the back wing is that its lift fluctuations were intensified with a significantly increased amplitude, where the rms value demonstrated an increase of approximately 30%, as shown in Table 1. In addition, Fig. 8 shows the frequency spectra of the lift coefficients for the tandem wings conducted using fast Fourier transform. The spectra of the back wing were more energetic than those of the front wing with higher amplitudes, which were closely associated with dramatic variations in the transient pressure fluctuations due to the upstream wake disturbances. The upstream wake interference amplified the instability and enhanced momentum mixing to energize the flow on the back wing. In the tandem configuration, the wakes from the upstream body provided the dominant source of instability for the downstream flowfield, resulting in more intensified fluctuations in the forces acting on the back wing. Regarding the extreme values of the transient forces, the lift of the back wing oscillated more drastically between the higher peaks

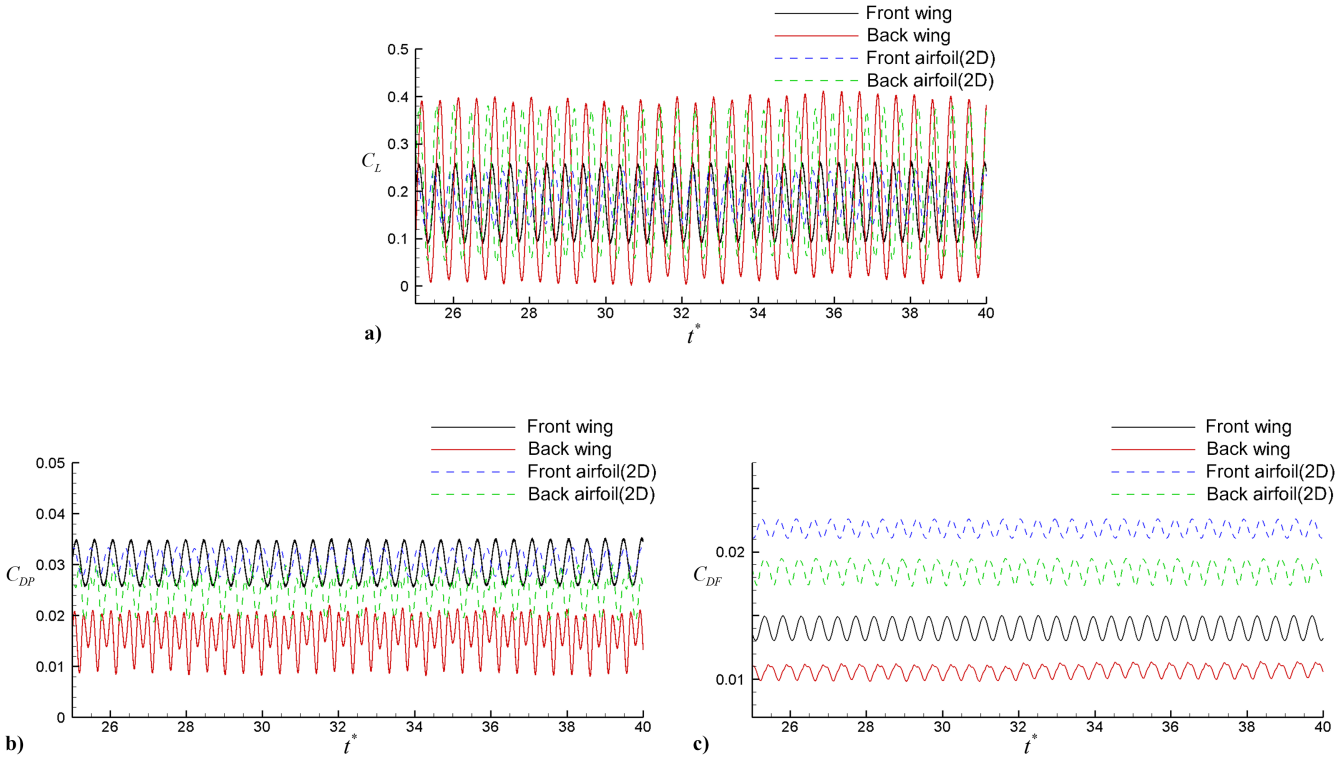

Fig. 7 Time histories of a) lift, b) pressure drag, and c) friction drag coefficients for the tandem wings overlaid with the 2-D case [28].

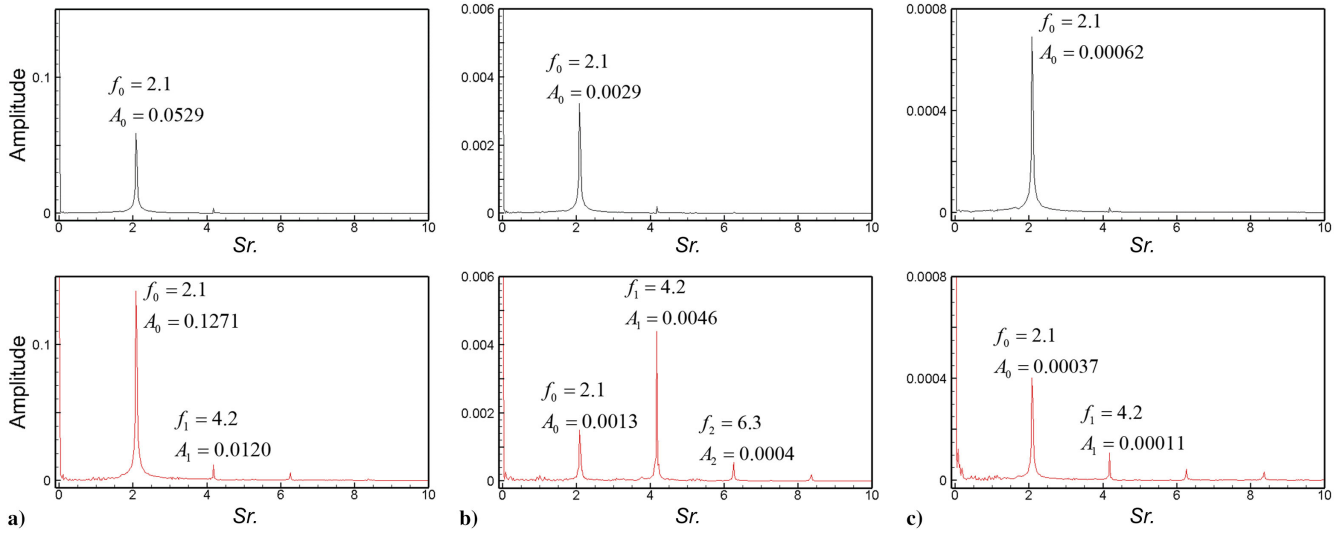

Fig. 8 Frequency spectra of a) lift, b) pressure drag, and c) friction drag coefficients for the front wing (top) and back wing (bottom).

and lower valleys than those on the front counterpart. Instead, the range of instantaneous drag on the back wing fluctuated below the corresponding forces of the front wing. However, the overall effect provided the back wing with a superior aerodynamic performance under incoming disturbances and vortex interactions. Therefore, it confirmed the conclusion of adding disturbances in [51] that the presence of disturbances may induce an aerodynamic performance enhancement with less requirement of energy input.

Apart from the intensified amplitude in the lift, the incoming disturbances and interactions also brought more distinct frequency modes into the flowfield around the back wing, as shown in Fig. 8. The force coefficients of the front wing presented a dominant single-frequency harmonic at $f_0 = 2.1$, which originated from vortex shedding around the trailing edge because most of the front wing was in a steady state, except the region in the vicinity of the wing tail. The base frequency of f_0 was generated by the primary instability generating the spanwise vortices in the flow around the trailing edge, which was confirmed by the simulation of an isolated NACA 0012 airfoil at approximately $Re = 1 \times 10^4$, with an equivalent wake shedding period at $T_0 = 1/f_0 = 0.48$ [52]. The phenomenon in this study is analogous to that of a previous investigation [27] in that the oscillating forces were regular and driven by the shedding of the von Kármán vortices from the laminar shear layers at the trailing edge, which brought about a narrow vortex street.

Notably, the flow over the back wing was mainly dominated by two modes at $f_0 = 2.1$ and $f_1 = 4.2$. The first mode f_0 was induced by a base frequency equal to the front wing, and the second higher mode of f_1 was twofold that of the base one. Analogous to the front wing, the spectra of the drag coefficients for the back wing presented relatively lower intensities than the lift oscillation. Meanwhile, the base mode f_0 dominated the lift and friction drag of the back wing. The spectra of pressure drag, however, revealed the dominant subharmonic f_1 prevailing over the base frequency f_0, which was different from that of the front wing. This explains why the pressure drag variation of the back wing in Fig. 7b displays a distinguished higher frequency fluctuation compared to that of the front wing. The higher-order harmonic was claimed to be related to the nonlinear effects of the vortices [53], which can be explained by the mathematical model applied in this study. Specifically, the nonlinear convection term $(\boldsymbol{U} \cdot \nabla)\boldsymbol{U}$ in the governing equation with the product term of velocities may give rise to the high-order harmonics. Supposing that the harmonic motion frequencies of f_a and f_b arise, for instance, via the primary instability, the nonlinear interactions of $\sin(f_a t) \cdot \cos(f_b t)$ or $\sin(f_a t) \cdot \sin(f_a t)$ can consequently emerge in the flowfield, and then the higher-order harmonics with frequency $(f_a + f_b)$ or $(2f_a)$ are induced in the nonlinear system. The nonlinear effect could explain the higher-order harmonic $f_2 = 6.3$ in the spectra of aerodynamic coefficients.

The temporal variations of the instantaneous aerodynamic coefficients reflect the prominent interacting features of the wings in tandem from the integration force perspective. To further investigate the mechanisms and flow details, coherent structures in the flowfield, particularly vortical structures, are the major subjects of interest in investigating the interactions between the tandem wings. In this study, the state-of-the-art Liutex-based VI method was applied to investigate the coherent vortical structures around the wings in the tandem flowfield. The explicit VI quantity of Liutex vector $\boldsymbol{R}$ is defined [54] as

$$\boldsymbol{R} = (\boldsymbol{\omega} \cdot \boldsymbol{r} - \sqrt{(\boldsymbol{\omega} \cdot \boldsymbol{r})^2 - 4\lambda_{ci}^2})\boldsymbol{r} \tag{6}$$

where λ_{ci} and $\boldsymbol{r}$ represent the imaginary part of the complex eigenvalue and the unit real eigenvector of velocity gradient tensor $\nabla \boldsymbol{u}$. The Liutex vector $\boldsymbol{R}$ provides the physical identification of the vortices in the flow in terms of rotational magnitude $R = |\boldsymbol{R}|$ and rigid rotation direction $\boldsymbol{r}$. Existing VI methods, such as the Q or λ_{ci} criterion, are based only on the scalar quantity to identify the rotational structures. These methods are normally dependent on the threshold value in practice. These quantities are all contaminated by the stretching and shearing effects, as proven in [34]. In this study, it is vital to accurately capture the vortex topology and direction to investigate the vortex evolution and vortex–wing interaction that mainly occurs in the shearing-dominated near-wall region. Therefore, the rigid rotation quantity of the Liutex vector is an ideal choice for representing the vortices, especially in the high-shearing boundary layers. In addition, based on the Liutex vector, the Liutex core line can be generated as a special Liutex vector line that passes the points satisfying the condition of $\nabla R \times \boldsymbol{r} = 0$. As elaborated by Xu et al. [55], the Liutex core line is a unique way to rigorously define vortex structures that physically represent the topology centers of vortices through their rotational axes. These state-of-the-art VI techniques were applied in this study to bring out the unique vortical topologies in the vortex–wing interactions in the following vortex structure analyses.

Next, the instantaneous vortical structure snapshots in Fig. 9 are considered to qualitatively present the typical features of spanwise vortices in the tandem configurations. These vortices were visualized by the isocontours of R_z, the spanwise-averaged component of the Liutex vector, where the negative value represents the clockwise spinning vortex V_c and the positive value represents the anticlockwise vortex V_{ac}. A variety of vortex features were detected and visualized in the wake shedding period of the front wing T_0 (Fig. 9), which included the Kelvin–Helmholtz (K–H) rolling-up vortices, wake shedding (zone A), bifurcated wake impinging onto the downstream geometry (zone B), wake-induced secondary vortices (zone C), wake–vortex interaction (zone D), and transition to turbulence wake (zone E).

Because of the K–H instability, the rolling-up 2-D vortices originated near the trailing edge of the front wing continuously propagating downstream until the gap region of the tandem-wing configuration. These were highly time-dependent events, with their time-averaged behaviors presented as a trailing-edge separation bubble on the front wing, as shown in Fig. 5. The majority of the front wing remained in the steady laminar state, whereas transition and separation were present near the vicinity of the trailing edge because of the onset of K–H instability. The contours of the spanwise-averaged TKE shown in Fig. 10 confirm that TKE reached the peak near the trailing edge of the front wing, where the vortices alternately shed into the tandem-wing gap region. The instability near the trailing edge was the sole source of the intensified turbulent fluctuations occurring in this region, which was strongly associated with the unsteady wake shedding of the

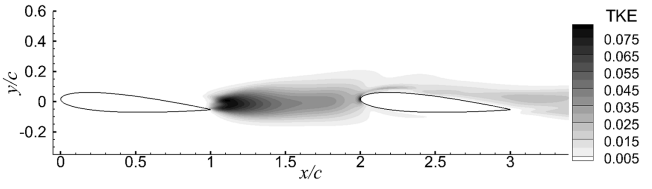

Fig. 10 Isocontours of the spanwise-averaged TKE distribution on tandem wings.

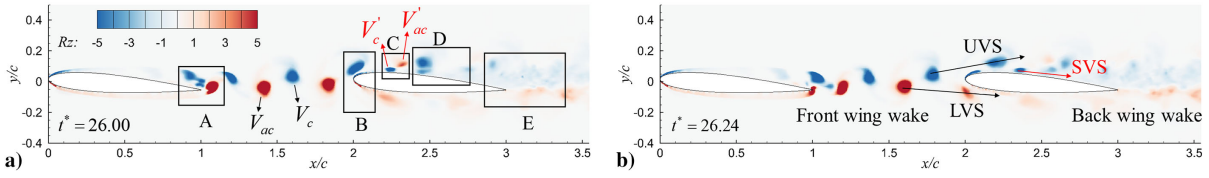

Fig. 9 Isocontours of the spanwise-averaged Liutex spanwise component at a) $t^* = 26.00$ and b) $t^* = 26.24$; five zones with typical vortex features are marked from A to E.

front wing. The oscillating forces on the front wing were solely attributed to the transient vortex shedding at the base frequency of f_0.

The von Kármán-type vortex street of the front wing maintained its coherence when propagating downstream until it approached the leading edge of the back wing, where the vortex street bifurcated into the upper vortex street (UVS) and lower vortex street (LVS) along the upper and lower surfaces of the wing, respectively (Fig. 9). The clockwise V_c and anticlockwise vortices V_{ac} from upstream were filtered by the back wing and traveled regularly on the upper and lower sides, respectively. Both UVS and LVS play dominant roles as sources of instability affecting the back wing to alter the vortex evolution topologies on the suction and pressure surfaces with varying degrees. On the suction side, as seen in zone C, the secondary vortices V_c' and V_{ac}' with the opposite sign of R_z were triggered after V_c in UVS propagated through the vertex point of the suction surface. This led to the near-wall secondary vortex street (SVS) traveling attached to the suction surface of the back wing. As the secondary vortex in SVS propagated downstream, V_c' and V_{ac}' gradually approached and interacted with the clockwise vortex in the UVS successively, resulting in the decay of V_{ac}' and the merging of the corotating vortices V_c and V_c'. These mutual interactions enhanced the 3-D destabilization and subsequent vortex deformation. Downstream of zone D, the merged vortices were distorted and disintegrated into the smaller turbulent structures in zone E, and eventually shed into the downstream turbulent wake. Moreover, the flow on the pressure side experienced comparatively less disturbance and instability and no sign of secondary vortex formation, as confirmed by Fig. 10, with a much lower TKE intensity on the lower side of the back wing. The instability on the pressure side was mainly from V_{ac} that impinged onto the back wing in zone B and was gradually distorted and disintegrated into the small-scale structures when traveling downstream.

A comparison between the upstream wake in zone A and the downstream wake in zone E suggests that the flow over the back wing was highly turbulent due to the continuous wake shedding from the front wing to the subsequent formation of the UVS, LVS, and induced SVS. The downstream mutual interactions and breakdown of vortices intensified the spanwise instability and accelerated the transition to 3-D structures in the flow. The vortex merging process of UVS and LVS also enhanced the turbulent mixing effect. The high-momentum fluid from the outer-layer UVS was entrained into the boundary layer in the inner-layer SVS to resist the flow separation on the back wing.

C. Three-Dimensional Vortex and Pressure Distribution

As we have already explored, it can be seen clearly that the incoming wake from the front wing induced the secondary vortices and led to intensive vortex interactions on the back wing. The triggered vortices observed in zone C (Fig. 9) were also reported to experience 3-D destabilization and breakup, giving rise to the bypass transition of the boundary layer [56]. Although the impact of the incident vortex street was mentioned and studied in the bluff body/wing interaction [25], the detailed vortical structures and their aerodynamic consequences have yet to be thoroughly examined due to their highly 3-D chaotic nature and intensive nonlinear interactions with the downstream body. The upstream wake, particularly UVS, not only brings in spanwise vortices causing the primary instability but also induces streamwise structures due to the intensified secondary instability, which plays an essential role in the coherent structures on the back wing and deserves careful investigation.

The 3-D panorama views of the instantaneous vortical structures occurring from the front-wing trailing edge up to the back-wing wake region are illustrated in Fig. 11, visualized by the isosurfaces of the Liutex vector magnitude $|\boldsymbol{R}| = 4$ colored by the spanwise and streamwise components, respectively. The 2-D primary and spanwise secondary instabilities are generally represented by the onset of spanwise and streamwise components R_z and R_x, respectively. These two typical topologies of vortical structures are distinctively present in the front-wing wake, which are the R_z-dominated spanwise wavy tube structure and the R_x-dominated streamwise coiling tube structure, referring to the spanwise vortex with the rolling axis in the z direction and the streamwise vortex with the spinning axis mainly in the x direction. The streamwise coiling tubes were aligned in the streamwise direction interweave with the spanwise wavy tubes, alternating between the positive and negative arc tube structures. The topology in the front-wing wake due to the secondary instability was similar to that of the Crow instability [57]. Meanwhile, the insets demonstrate the tangling details of the vortices in the back-wing wake, featured by the highly 3-D, multiscale, and turbulent structures. Unlike the front-wing wake with noticeable spanwise and streamwise structures, the wake on the back wing is suppressed due to the incoming interference, and no sizable vortices are formed in this turbulent region.

As presented in Fig. 11, the well-organized spanwise tubes interconnected by the streamwise coiling tubes were maintained in the gap region until being bifurcated by the back-wing body into UVS and LVS. During this process, the counter-rotating spanwise wavy tubes gradually enlarged their streamwise intervals, leading to the stretching and elongation of the streamwise coiling tubes. When reaching the back wing, the streamwise coiling tubes were separated following the bifurcated spanwise rollers along UVS and LVS. The rollers in UVS became wavier in the streamwise direction due to the increased secondary instability and then broke down into fully 3-D structures after merging with the secondary vortices downstream in zone D. On the lower side, however, the anticlockwise roller V_{ac} in LVS impinged onto the leading edge of the back wing and then underwent severe distortions. Therefore, the flow pattern on the lower surface of the back wing was relatively simple in that the upstream spanwise roller and coiling streamwise tube were rapidly disintegrated into small vortical structures as they were shed into the wake.

Because of the interferences of the upstream wavy tube and coiling tube, coherent structures are noticeable on the suction side of the back wing. The triggered counter-rotating secondary vortices V_c' and V_{ac}' initially present the distinct spanwise structures in the inset of Fig. 11a, similar to the spanwise rollers generated near the trailing edge of the front wing due to the K–H instability. The topology of the wake-induced vortices is similar to that formed on the flat-plate boundary layer reported in [56,58]. Wang and Wang and Wang et al.

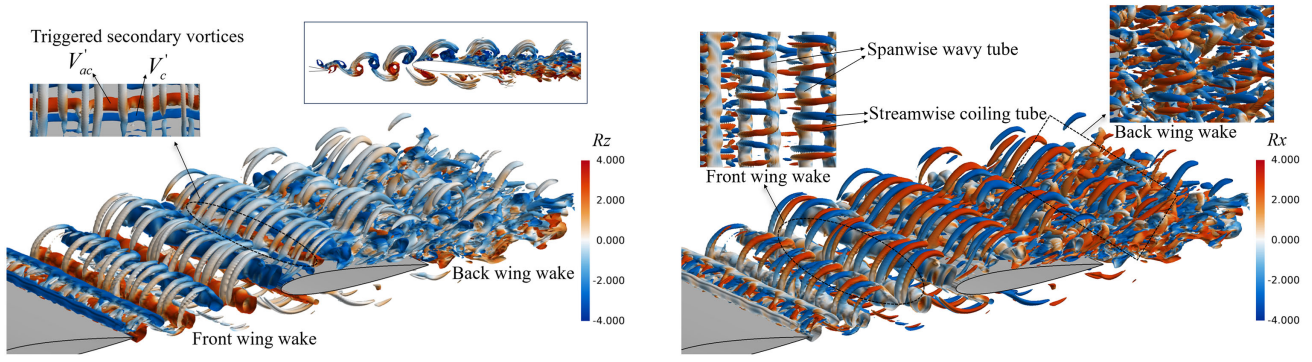

Fig. 11 Isometric view of the isosurfaces of Liutex magnitude $|R| = 4$ colored by the a) spanwise component R_z and b) streamwise component R_x, with the side and top views in the insets.

[59,60] found the double induced vortices with the same spanwise rotational direction generated in the boundary layer in a multi-element airfoil and a cylinder–airfoil configuration. However, the secondary vortices in the current tandem configuration were found to be the counter-rotating vortex pair with opposite spanwise spinning directions in the boundary layer of the back wing. As the induced secondary vortices propagated further downstream, the initial spanwise topology changed drastically in the subsequent transition process on the suction surface. The vortices gradually evolved into 3-D structures and eventually broke down into smaller-scale structures due to the intensified secondary instability and perturbation introduced by the outer-layer UVS. Marxen et al. [61] reported that the elliptical instability of the vortex leads to its spanwise deformation, whereas another instability between consecutive vortices leads to disintegration. The close 3-D top views on the suction side of the back wing at the time-sequential instants in Fig. 12 provide the typical topology evolution process of the induced secondary vortices visualized by the isosurfaces of Liutex magnitude $|R| = 4$ and by applying the Liutex core line [55] to capture the rotational axes of these vortex structures. The Liutex core line is represented by the white line superimposed by the Liutex isosurfaces in the detailed view of Fig. 12. It identifies the vortex topology with the core line as the spinning center when propagating downstream on the back-wing wall surface. The 3-D vortex evolution process is mainly found in three stages of typical topologies when these secondary vortices move downstream from the leading edge to the trailing edge until they shed to the wake.

In the initial stage I, the boundary layer near the leading edge was disturbed by the upstream spanwise and coiling tubes, which led to the generation of the clockwise secondary vortex V_c' in the vicinity of the leading edge. The initial topology of V_c', as shown in Fig. 12a, took the pattern of nearly a 2-D spanwise tube with little streamwise meandering. When the clockwise vortex $V_{c'}$ propagated downstream (Fig. 12b), another counter-rotating secondary vortex V_{ac}' was then generated in the outer layer quite close to the V_c' as a vortex pair. The amplified disturbances and the accompanying 3-D destabilization led to the induced vortex pair being deformed and wavier in the streamwise direction. With the distorted rollers rolling downstream, the initial streamwise rotation emerged. The two initial spanwise tubes were deformed into 3-D wavy vortical structures in late stage I.

In stage II, as shown in Fig. 12c, the enhanced secondary instability caused the spanwise wavy tubes to continue to deform in the streamwise direction until they disintegrate into multiple isolated Λ-shaped vortices. The disintegration and breakup processes were caused by the spanwise deformation of vortices and the formation of streamwise structures [62]. The streamwise component R_x of the Liutex vector was dominant in the Λ vortices instead of the spanwise component R_z. These Λ vortices were characterized by their distinctive spanwise wavelengths of instability, similar to the findings reported by He et al. [63] for a simplified cylinder/flat-plate configuration. In the downstream propagation, with the Λ vortex being convected downstream in Fig. 12c, its head was gradually lifted away from the wall surface, and its tails further descended down to the wall, leading to the legs of the Λ vortex being elongated streamwise.

Thereafter, in stage III, hairpin-shaped vortices were formed when the Λ vortex was elevated and then interacted with the outer-layer UVS coming from upstream, as visualized in Fig. 12d. The streamwise strength was enhanced, and the distances between the hairpin

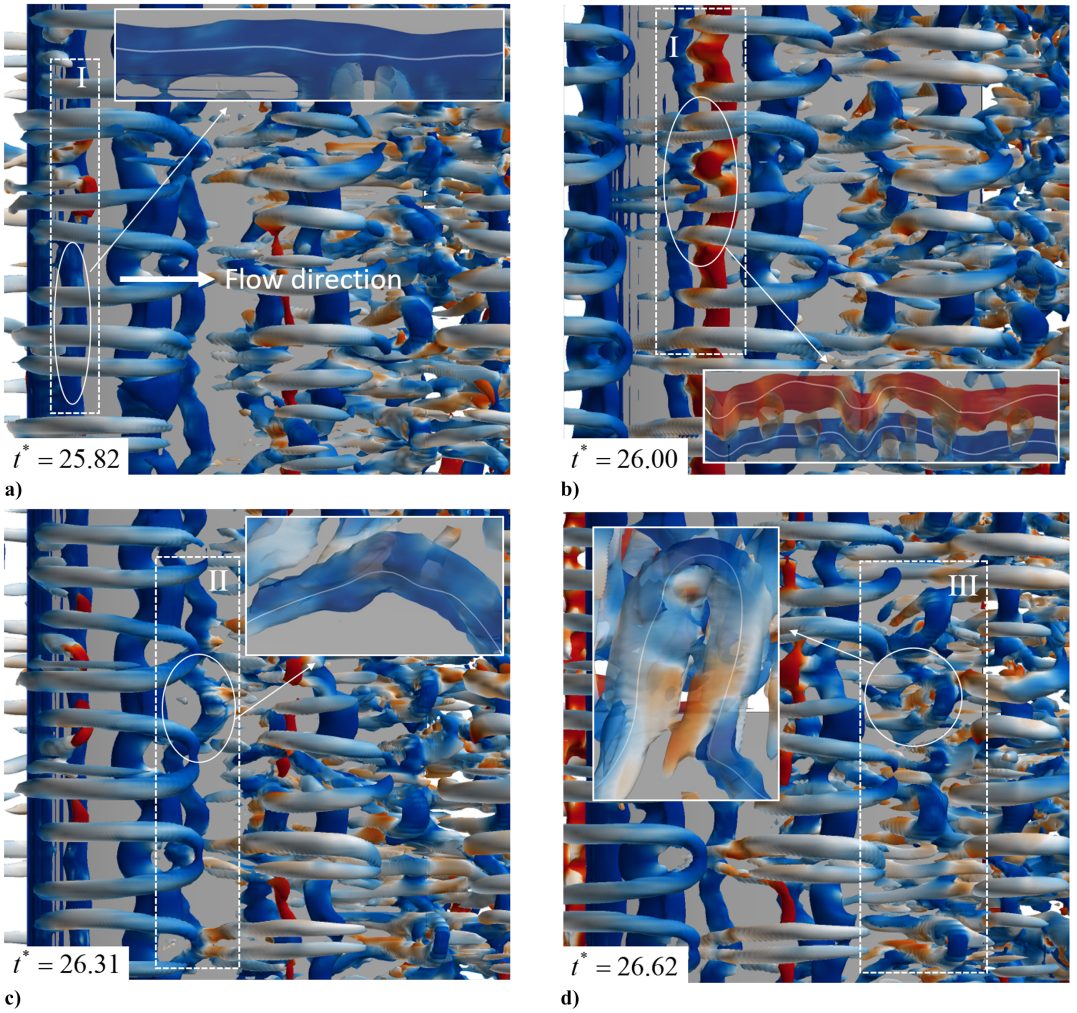

Fig. 12 Top view of the secondary vortex evolution on the back wing visualized by the Liutex magnitude isosurfaces, and the close-up insets show the typical vortex topology superimposed by the Liutex core line in white.

vortex legs were reduced when evolving downstream. The intensive vortex interactions between UVS and SVS in stage III further enhanced the 3-D instability, thereby inducing a variety of smaller disintegrated breakdown vortices. When traveling downstream, hairpin vortex packets and breakup streamwise vortices were generated near the suction wall surface and shed into the wake region beyond the trailing edge. Unlike the front-wing wake, the wake of the back wing did not exhibit noticeable spanwise and streamwise structures, and these structures were more 3-D and multiscaled. The strong wake disturbances continuously and periodically enhanced the momentum mixing and 3-D nonlinear instability by triggering double secondary vortices and subsequent interactions to sustain the turbulent flow and prevent the formation of large-scale vortices on the trailing edge of the back wing.

In the three stages, from vortex generation to shedding into the wake, the secondary vortex near the boundary layer underwent vortex merging and breakdown. The 3-D deformation of the vortex topology in the evolution distinctively affected the velocity and pressure distributions on the wing. Three typical vortex topologies in the evolving process, with their local pressure distribution and related velocity vector plot colored by the Liutex magnitude R on the spanwise slices of the y-z plane are illustrated in Fig. 13. For the spanwise tube in stage 1 (Fig. 13a), no visible streamwise rotation was found in the slice. The high- and low-pressure regions exhibited a banding distribution in the spanwise direction, highlighted by the rapid change in the vertical direction of the Liutex magnitude R. As the vortex propagated downstream, the streamwise structures emerged from the initial Λ-shaped vortex to the subsequent hairpin vortex, where the visible rotational motions are presented in the spanwise slices in Figs. 13b and 13c. The rotation center was located in the streamwise structure, with the local maximum of R coinciding with the local minimum of pressure. The pairs of low-pressure regions concentrated in the vortex legs were lifted, and the low-pressure centers were approaching, following the vortex evolution process from the Λ vortex in stage II to the hairpin vortex in stage III. For vortices with different topologies, the 3-D vortex evolution and deformation led to variations in the spanwise pressure distribution, as the low-pressure area was always highly correlated to the vortex rotation center and the location of the Liutex core line. The relationship of the vortex topology with the pressure distribution suggests that the vortex evolution on the wing is closely associated with and consequently results in variations of the aerodynamic performance.

D. Power Spectral Density Characteristics

Because of the interferences and interactions from the wake of the front wing, the flow over the back wing experienced intensive primary and secondary instabilities. The periodic spanwise wavy tubes and streamwise coiling tubes presented prominent spatial and temporal characteristics that affected the coherent structures on the back wing, especially the induced secondary vortices. Therefore, the spatial and temporal behaviors of the induced vortices in the evolution stages (Fig. 13) of the back wing influenced by the upstream wake were of interest in this study. The power spectral densities (PSDs) were quantitatively analyzed using the spanwise and streamwise components of the Liutex vector. Welch's modified periodogram method was applied to calculate the spectra, and these PSD features were compared between the different locations on the back wing to understand the characteristics of the tandem interactions.

The spatial PSDs examined the spanwise distributions of the Liutex streamwise component R_x of the vortices, as shown in Fig. 14. The wave number k corresponding to the peaks in the spatial PSDs provided an estimation of wavelength $\lambda_z = 1/k$ for the streamwise modes in the coherent structures. The spanwise

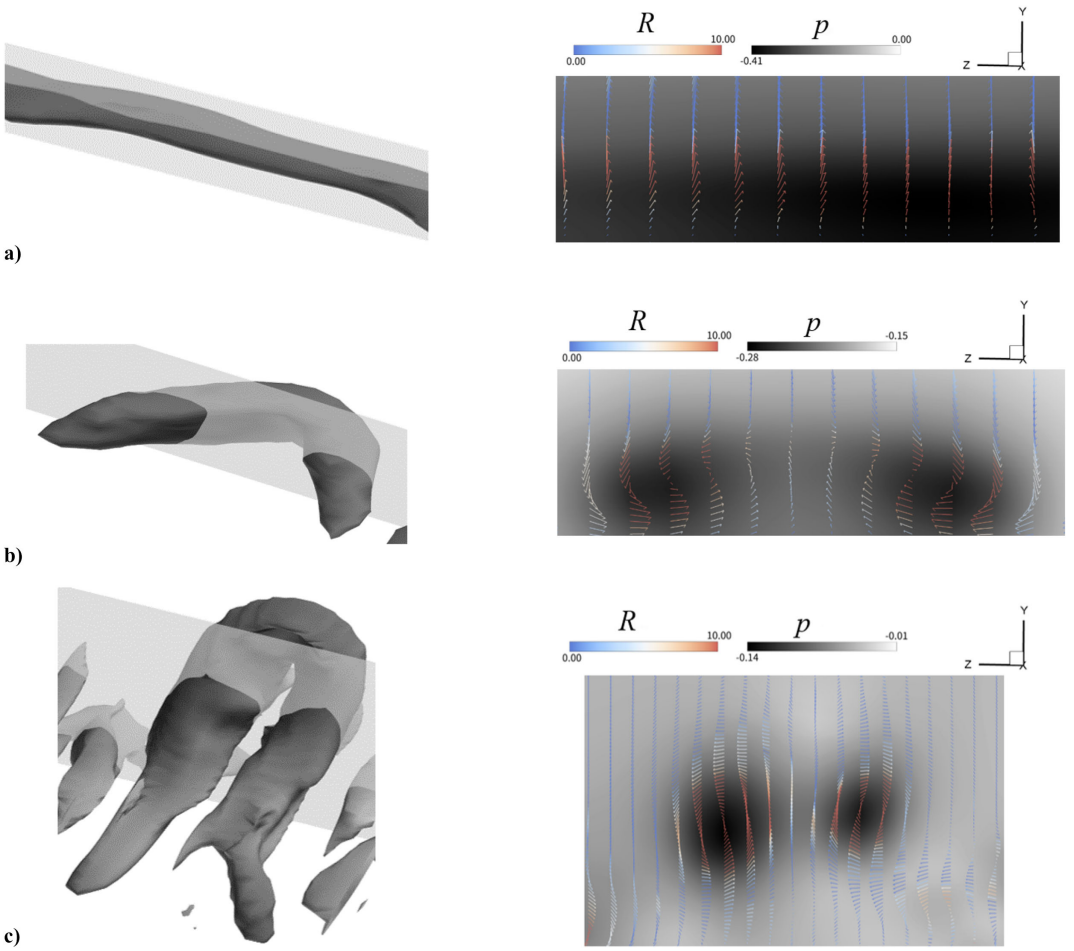

Fig. 13 Typical topology of a) spanwise tube, b) Λ vortex, and c) hairpin vortex with the pressure contour and velocity vector plot colored by the Liutex magnitude $|R|$ on each spanwise slice.

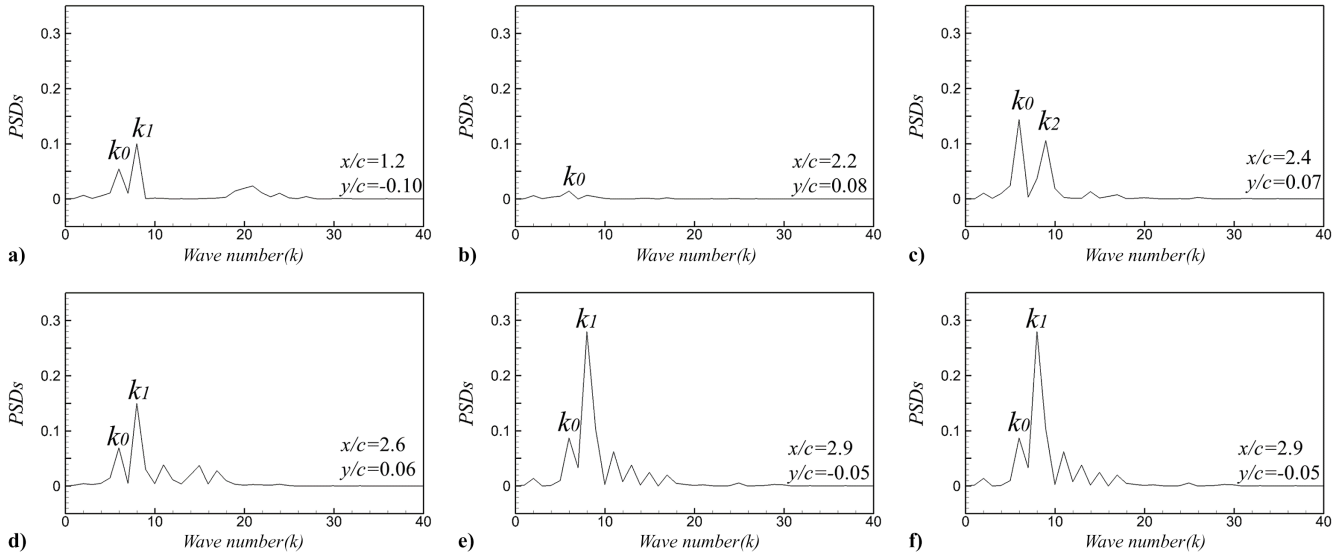

Fig. 14 Spatial PSDs of streamwise Liutex component R_x along the wingspan: a) at the front-wing wake and b–f) on the suction surface of the back wing, marked with the dominant wave numbers $k_0 = 5.97$, $k_1 = 7.97$, and $k_2 = 8.97$.

wavelength λ_z represents the characteristic gap sizes in the spanwise direction between two consecutive vortical structures. The spatial PSDs along the span at different streamwise locations are set on the suction side of the back wing, where the position coordinates $(x/c, y/c)$ were at the secondary vortex formation (2.2, 0.08), early transition (2.4, 0.07), late transition (2.6, 0.06), trailing edge (2.9, –0.05), and wake (3.2, –0.1). In addition, the PSDs at the front-wing wake (1.2, –0.1) as the baseline are shown in Fig. 14a.

Noticeable peaks in the spectra of the front-wing wake occurred at wave numbers of $k_0 = 5.97$ and $k_1 = 7.97$, as shown in Fig. 14a, which indicates that the typical wavelengths of the front-wing wake were approximately at $\lambda_{z0} = 0.167$ and $\lambda_{z1} = 0.125$. The dominant spanwise wavelength λ_{z1} is consistent with the observation of the time-averaged recirculation area boundary of the front wing (Fig. 6). Regarding the induced vortices on the back wing, SVS originated near the arch point of the wing in the form of spanwise tubes. The spectra at this location were quite weak due to the spanwise dominance and streamwise weakness of the initial secondary vortices in stage I. However, it is still visible in Fig. 14b that the initial spanwise instability of the induced vortices was at a major wavelength of $\lambda_{z0} = 0.167$. Thereafter, in the early transition, these spanwise vortices rapidly deformed into the streamwise structures of Λ shape in stage II. It can be noticed that the k_0 in the initial structures exhibited increasing amplitude in the spectra due to the intensified secondary instability, which still played the lead role in PSDs of the early transition. In addition, a different higher mode $k_2 = 8.97$ was observed at this stage, as shown in Fig. 14c. When propagating downstream and merging with UVS in the late transition, the vortices deformed into hairpin-shaped patterns in stage III. The dominant wave-number mode turned into $k_1 = 7.97$ (Fig. 14d), which is consistent with the dominance in the front-wing wake. Accordingly, the dominant secondary instability wavelength was approximately at $\lambda_{z1} = 0.125$ in the late transition after mutual interactions. The wavelength of k_1 was initially present at the late transition $x/c = 2.6$, which was related to the formation of the 3-D separation bubbles near the trailing edge (Fig. 6). The dominant spanwise wavelength for the vortices is consistent with the spanwise distribution of the separation bubbles. As the hairpin vortices propagated downstream with disintegration, the wave-number mode k_1 became completely dominant when the transition approached the trailing edge and back-wing wake zone. The amplified dominance of k_1 in the spectra and its associated enlargement of the recirculation bubbles downstream up to the trailing edge gave rise to the intensified 3-D destabilization near the boundary due to the vortex interactions.

The temporal PSDs of the vortices were investigated for both the front and back wings in the streamwise direction by placing the probe points near the wing surfaces and collecting time-sequential simulation data at these points. Figure 15 presents the temporal PSDs at five probes (P0–P4) with their locations around the tandem wings. The probe P0 was set at the front-wing wake as the baseline, and the amplitude of the spectra for each successive probe from P1 to P4 close to the back wing was stepped by 10^5 of magnitude. The spanwise-averaged spectra of the spanwise component of the Liutex vector R_z were obtained to investigate the frequencies of dominant streamwise propagation motions. All probe data were collected over 40 time units covering approximately 100 upstream wing wake-shedding period cycles. The power spectra at these probes (Fig. 15) display a complex distribution with multiple frequency peaks.

As the baseline probe in the front-wing wake, the spectra of P0 detected a major peak at $f_0 = 2.1$ and a couple of subharmonics at f_1 and f_2, which suggests that the upstream wake sheds at the frequency of f_0 and the subharmonics are generated by the nonlinear interactions in the flow. The dominant frequency in the front wake was consistent with that in the spectra of the aerodynamic forces of the front wing (Fig. 8), which explains that the variations in aerodynamics on the front wing are mainly driven by periodic wake shedding. Yarusevych et al. [27] reported that the similarity exists in the airfoil wake at low Reynolds numbers with a universal scaled Strouhal

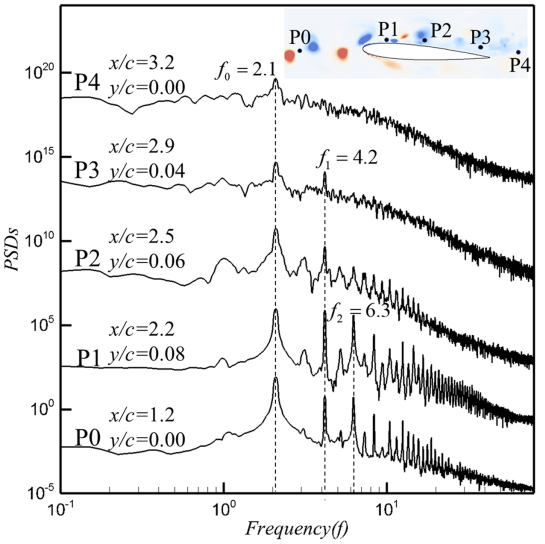

Fig. 15 Temporal PSDs of the spanwise Liutex component R_z for probes from P0 to P4, with the amplitude magnitude successively stepped by 10^5 for clarity.

number Sr^* calculated by the wake shedding frequency f_s and the vertical distance between two vortices in the near-wake region d^*. For the front wing in the current tandem layout, the scaled wake shedding Strouhal number was found at $Sr^* = 0.165$, which was consistent with the universal Strouhal number of $Sr^* \approx 0.17$ at low-Reynolds-number regimes [27].

For the probes on the back wing, two distinct peaks at f_0 and f_1 were identified in the spectra of P1–P4, in accordance with the two frequency modes found in the spectra shown in Fig. 8. It was speculated that the force variations on the back wing were related to vortex propagation, mutual interaction, and the evolution process along the wing surface. The induced secondary vortices generated near P1 produced peaks with almost comparable amplitudes for the base frequency f_0 and higher harmonics f_1 and f_2 in the spectra. Subsequent interactions between the upstream wake and secondary vortices near P2 exhibited a distinct peak at the base frequency f_0, whereas the amplitudes at the higher subharmonics experienced a dramatic decrease. The spanwise dominance in the vortices gradually declined due to the enhanced secondary instability, and the periodic characteristics of the primary instability weakened accordingly. Further downstream to the trailing edge, the vortices gradually broke down into small-scaled 3-D structures, and the amplitudes of the spectra declined gradually at both f_0 and f_1. No apparent subharmonic peak was detected in the downstream wake at P4, and the spectra of the downstream wake featured a weak single peak at f_0. Unlike the front-wing wake, no pronounced periodicity of vortices was observed in the back-wing wake.

E. Vortex Evolution and Aerodynamic Force Variations

Zhang et al. [1] pointed out that the separation suppression due to the inflow wake excitation caused the increased lift in the time-averaged flowfield. The phenomenon of the separation suppression effect is similar to the results of this study, as presented in Fig. 5, and is in agreement with previous findings [60,64]. However, the time-averaged results can only reflect the mean aerodynamic behaviors of the tandem wings instead of their time-dependent performance. Given the current DNS data, a detailed investigation was performed to reveal aerodynamic performance enhancement mechanisms from the perspective of transient multiscale coherent structures in the flowfield. As mentioned in the preceding section, the aerodynamic force coefficients are inherently influenced by the coherent structures around these wings, resulting in distinctive aerodynamic interactions in the tandem-wing configuration. More specifically, the aerodynamic force variations with time (Fig. 7) indicate that the instantaneous lift coefficient of the back wing is not always superior to that of the front wing at all time instants, which only occurs in limited time periods in a cycle. Therefore, it is interesting to study the lift augmentation mechanisms by investigating the footprints of these coherent structures and aerodynamic force variations to better understand the role of these vortices in aerodynamic interactions.

A more detailed study of the forces was provided in an oscillating cycle for the tandem wings, in which the variations in aerodynamic forces were explored in a typical cycle and their correlations with the vortex patterns on the tandem wings. The time-sequential snapshots of the coherent structures and their corresponding lift and drag coefficients are depicted at typical instants in a dominant wake shedding period T_0 for the front wing as the uniform inflow baseline in Figs. 16 and 17; and for the back wing in Figs. 18 and 19 as the targeted study with the incoming wake disturbances. The chosen time instants for the front wing (Fig. 16) and the back wing (Fig. 18) were the force coefficients characterized at the local high and low peaks and mean values. Moreover, the vortex patterns identified by the Liutex component R_z and the corresponding surface pressure distribution C_p around the front and back wings are shown in Figs. 17 and 19, respectively, to perform the following correspondence analysis.

For the front-wing baseline presented in Fig. 16, the lift and drag variations synchronously oscillated at the base frequency governed by the natural cyclic vortex shedding resulting from the primary instability featured with the spanwise vortices. The temporal sequential event began with the maximal lift and drag at instant *i* when the clockwise vortex started to shed off from the trailing edge of the suction surface, and the anticlockwise vortex began to form on the trailing tip near the pressure surface, as shown in Fig. 17a. The temporal sequence ended at instant *v* in Fig. 17e, when a new wake-shedding cycle and the vortex-shedding pattern repeated the periodic event at the instant *i*. The instantaneous pressure contours and pressure coefficient distributions in Fig. 17 show the pressure variations on the front wing from instant *i* to *v*. Based on the sequential vortex evolutions and the related pressure fields in Fig. 17, the correspondence analysis conducted between the force coefficients and vortex patterns on the front wing focusing on the five representative instants is explained as follows.

At instant *i*, the clockwise vortex V_{c1} on the trailing edge of the suction side developed and was about to leave the tip to shed into the wake. Meanwhile, a tiny anticlockwise vortex V_{ac1} emerged right at the trailing-edge tip. At that moment, the front wing experienced maximum lift and pressure drag, with a nearly minimum viscous drag. The maximal lift resulted from the higher pressure on the lower surface and the lowest pressure on the upper surface, as shown in Table 2. From then on, the anticlockwise vortex V_{ac1} grew rapidly attached to the tip from instant *i* to *iii* when the matured vortex left the trailing tip and propagated into the wake. On the suction side, a weak clockwise rolling-up vortex V_{ru} was generated and then traveled downstream along the wing surface. An instantaneous rolling-up vortex structure was formed due to the flow separation, and the structure is illustrated as a trailing-edge laminar separated bubble from the time-averaged perspective shown in Fig. 5a. Kirk and Yarusevych [62] found that the laminar separated bubble was a time-averaged structure of unsteady separation, which mainly resulted from the coherent structures rolled up by the separated shear layer. From instant *i* to *iii*, the pressure on the upper surface increased to its maximum, whereas that on the lower surface decreased. Therefore, the growing anticlockwise vortex V_{ac1} at the trailing tip was accompanied by an enlarged area of decreased pressure on the lower surface near the trailing edge. At instant *iii*, the matured anticlockwise vortex V_{ac1} at the tip was about to shed into the wake when the pressure on the lower surface reached its minimum, resulting in the

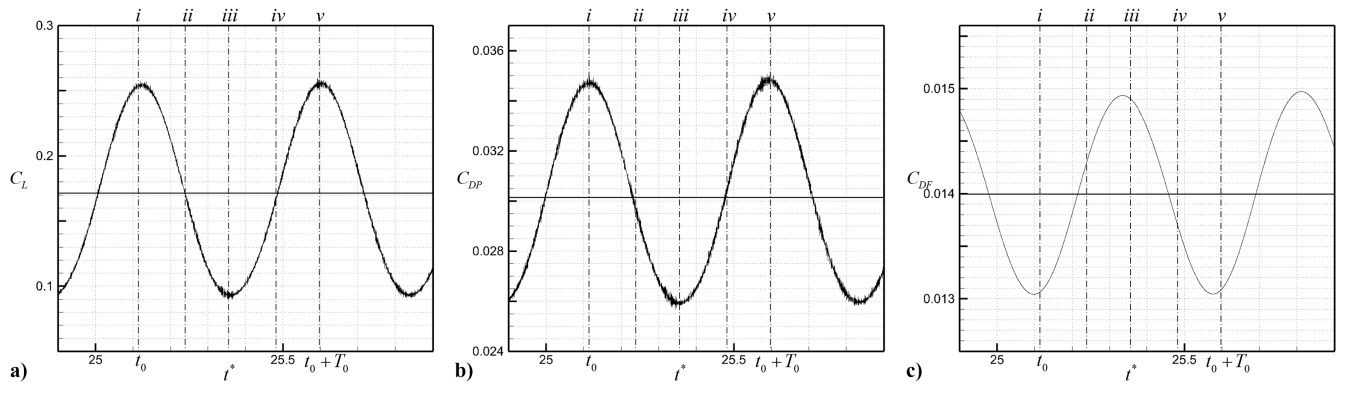

Fig. 16 Time histories of a) lift, b) pressure drag, and c) friction drag coefficients for the front wing in a period T_0 with five selected instants from *i* to *v* marked from left to right.

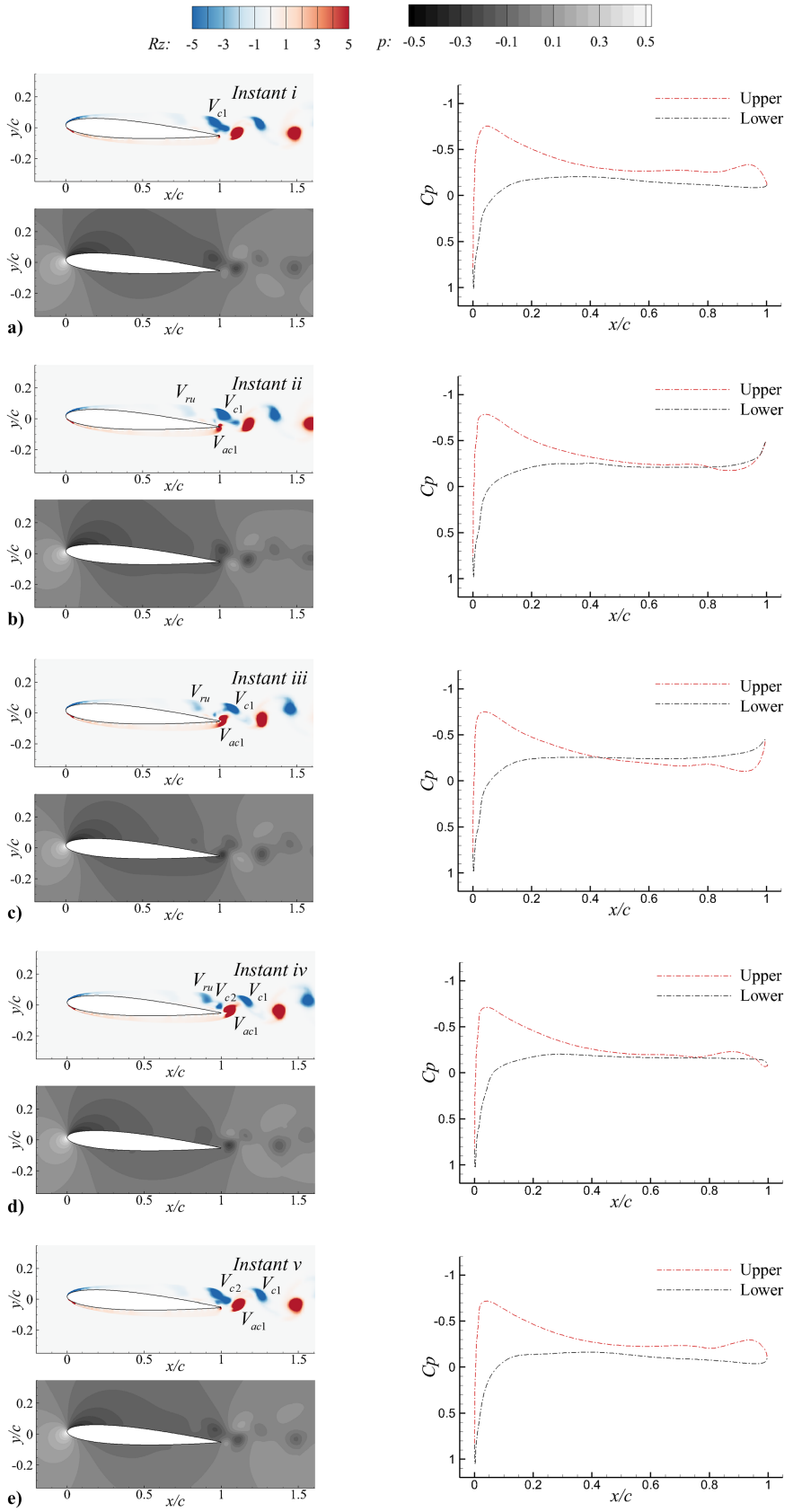

Fig. 17 Isocontours of the spanwise Liutex component and pressure distribution (left) and the surface pressure coefficient distribution (right) of the front wing at five selected instants *i* to *v* from a) to e) in sequence.

minimum lift and pressure drag with a nearly maximized viscous drag. The local negative lift was covered from $x/c = 0.4$ to $x/c = 1.0$, nearly up to 60% of the entire chord near the trailing tip. During instants *iii* to *v*, the rolling-up vortex V_{ru} continued to travel downstream toward the trailing tip. Another new clockwise vortex V_{c2} arose and stagnated at the trailing edge on the upper surface. When the time instant marched to *v* as the rolling-up vortex V_{ru} was getting close to the trailing edge, it merged with the clock-

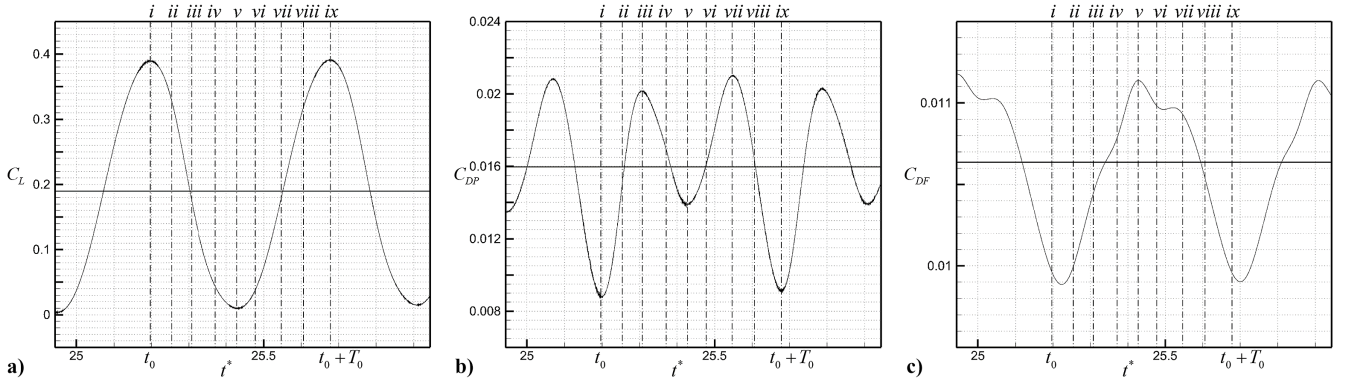

Fig. 18 Time histories of a) lift, b) pressure drag, and c) friction drag coefficients for the back wing in a period T_0 with nine selected instants from *i* to *ix* marked from left to right.

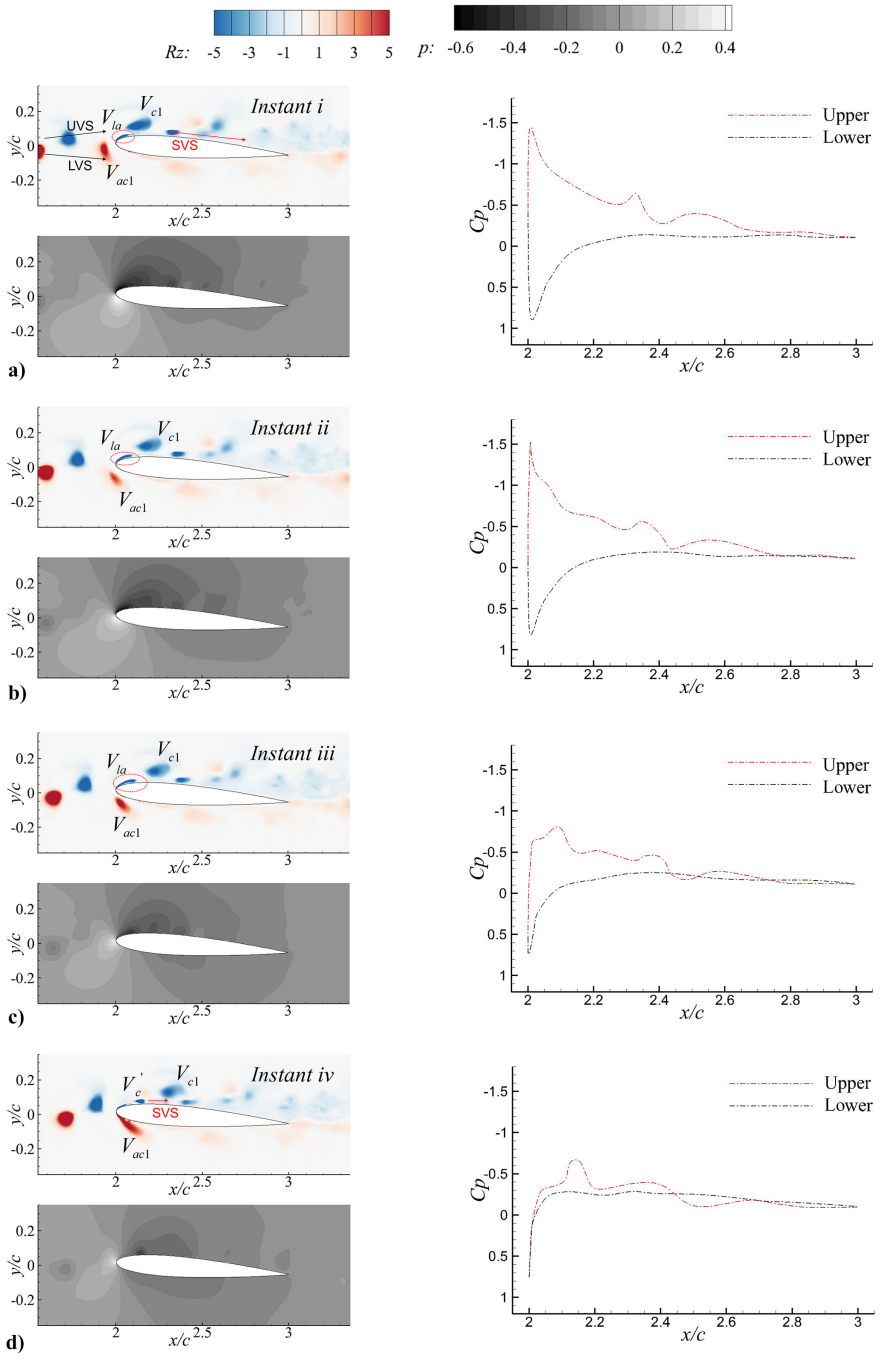

Fig. 19 Isocontours of the spanwise Liutex component and pressure distribution (left) and the surface pressure coefficient distribution (right) of the back wing at nine selected instants *i* to *ix* from a) to i) in sequence.

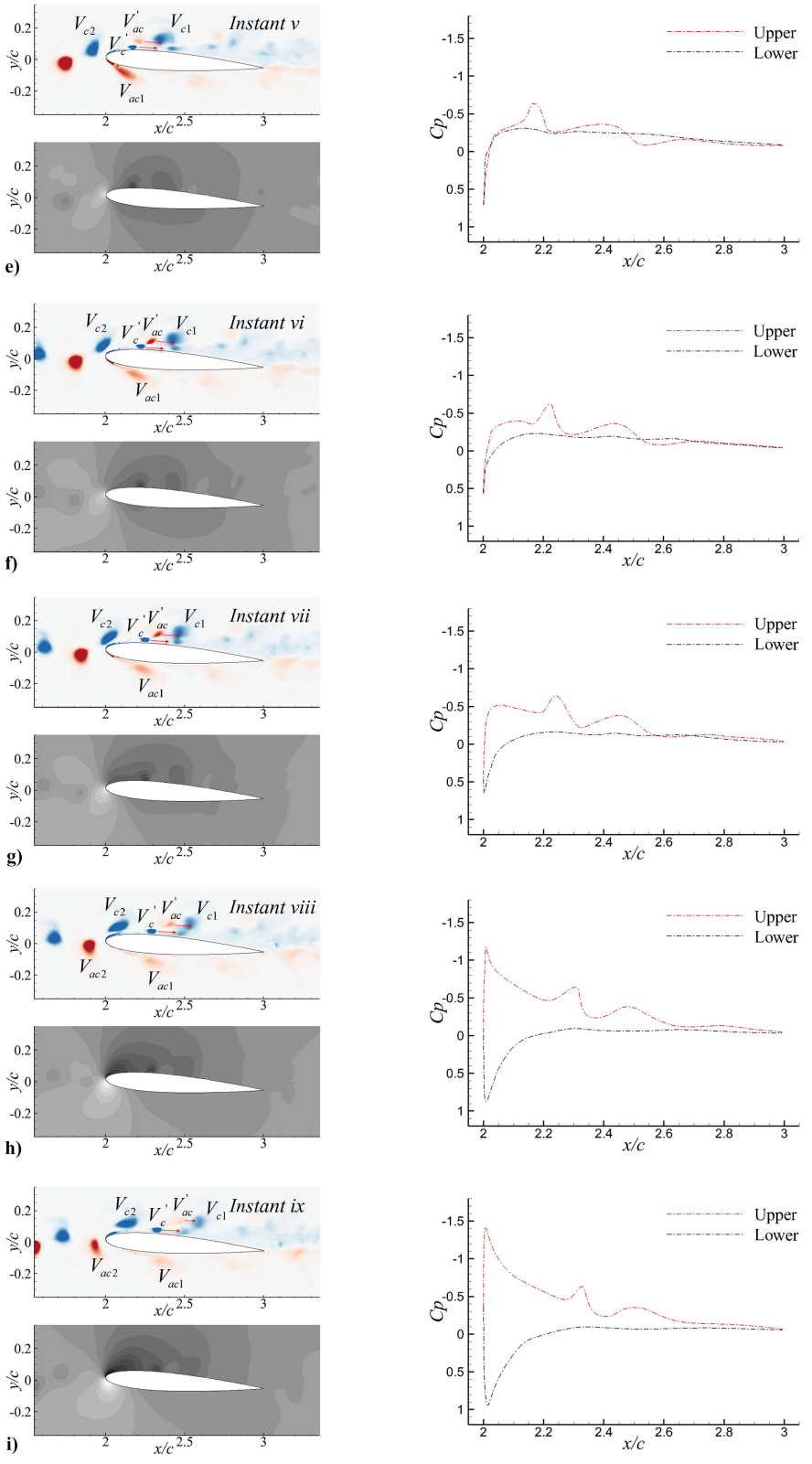

Fig. 19 (Continued).

wise vortex V_{c2} into a larger and matured clockwise vortex, which was ready to shed into the wake paired with the anticlockwise vortex V_{ac1} in the gap and then repeated the periodic scenario at instant *i*. The pressure on the upper surface gradually decreased during this process, as shown in Table 2, following the enhanced clockwise vortex on the suction side.

The corresponding spanwise-averaged integrated pressure coefficient on the upper and lower surfaces of the front wing was closely linked to vortex formation and shedding events on the trailing edge. Remarkably, the local maximum and minimum lift and pressure drag were always associated with instantaneous low-pressure events near the wingtip. The lift peak occurred when the clockwise vortices dominated near the trailing tip, and the valley occurred when the anticlockwise vortices played the leading role. As a result, the lift and pressure drag variations on the front wing were closely linked with the counter-rotating vortex pairs that were alternately generating and

Table 2 Spanwise-averaged pressure coefficient on the upper/lower surface and lift coefficient for the front wing at five typical instants

Instant	*i*	*ii*	*iii*	*iv*	*v*
C_p (upper)	−0.3700	−0.3594	−0.3058	−0.3007	−0.3304
C_p (lower)	−0.1160	−0.1902	−0.2125	−0.1318	−0.0754
C_L	0.2539	0.1693	0.0933	0.1689	0.2550

shedding on the trailing tip, accompanied by the propagation of the low-pressure area near the trailing edge. It is convincing that the aerodynamic performances on the front wing were solely attributed to and are closely bonded to the transient behaviors of large-scale vortex structures near the trailing edge.

The lift and drag fluctuations of the back wing were found to be different from those of the front wing, particularly the pressure drag signals with prominent multipeaks and valleys in a period, as shown in Fig. 18. Compared to the baseline of the front wing, the vortex streets from the upstream wake caused periodic disturbances to the back wing, leading to a complex vortex system and interactions with amplified instabilities, higher-frequency harmonics, and associated vortex perturbations. The evolution of the vortex system past the back wing was investigated in an upstream wake shedding period T_0, during which these upstream vortices V_c and V_{ac} alternately passed the leading edge and propagated through the upper and lower surfaces of the back wing, which gave rise to the two distinctive vortex streets with different AVI characteristics in UVS and LVS, respectively. Nine typical instants were selected to investigate the time-sequential vortex evolution and pressure variations on the back wing (Fig. 19). The corresponding instantaneous surface pressure coefficients on the upper and lower surfaces are listed in Table 3.

The time-sequential snapshots in the front wake shedding period T_0 began with instant *i* when the upstream clockwise vortex V_{c1} traveled across the leading edge and reached the vertex point of the wing profile, as shown in Fig. 19a. Meanwhile, the anticlockwise vortex V_{ac1} approached the leading edge. The clockwise vortex V_{c1} triggered the generation of the leading-edge attached vortex V_{la} on the back wing. At this instant, the lift of the back wing was at its maximum, whereas contrary to the baseline scenario, the pressure drag presented its first local minimum. From then on until instant *iii*, the lift on the back wing began to decline near its mean value, whereas the pressure drag increased to the first local maximum. The leading-edge attached vortex V_{la}, marked by the red circles in Fig. 19, was stretched along the streamwise direction by the vortex in UVS traveling downstream, leading to the generation of a secondary vortex near the surface. Accordingly, the low-pressure peak on the upper surface near the leading edge gradually diminished and eventually vanished at instant *iii*, as shown in Fig. 19c. This was because the high-pressure zone near the back wing transferred from the lower surface to the leading edge, and the low-pressure zone on the suction side gradually weakened. Instead, a new adverse pressure zone providing the extra low pressure arose near the location at $x/c = 2.1$, where exactly the secondary vortex in SVS detached from V_{la}. The emerging low-pressure region near the leading edge further migrated downstream following the secondary vortex V_c' propagation on the suction surface. Meanwhile, the surface pressure gradient on the lower surface experienced an evident increase near the leading edge from $x/c = 2.0$ to $x/c = 2.1$, as shown in Figs. 19d and 19e, as the V_{ac1} went close to the back wing and impinged onto its leading edge. This was also due to the migration of the high-pressure area on the lower side, which led to a pressure decline on the lower surface. From instant *iii* to *v*, the lift and pressure drag declined simultaneously until the lift reached its minimum and the pressure drag reached its second local minimum.

Alternately starting from instant *v* with the minimal transient lift in Fig. 19e, the upstream V_{c2} approached close to the leading edge on the wing upper side, and V_{ac1} was underway to disintegrate after impinging onto the back wing from the lower side. The lift in this moment was provided by the secondary vortices attached close to the upper surface at $x/c = 2.1$ and $x/c = 2.4$. The pressure on the upper side reached its maximum, and the pressure on the lower side decreased to its minimum. With the anticlockwise vortex V_{ac1} propagating downstream away from the leading edge, the high-pressure area on the leading edge began to migrate back to the lower surface. Accordingly, the increased pressure gradient near the leading edge decreased to enhance the pressure on the lower surface. The lift returned to the average, and the pressure drag climbed to the second local maximum at instant *vii*. From instant *vii* to *ix*, the low-pressure peak was regained at instant *viii* when the next upstream clockwise vortex V_{c2} approached the back-wing profile, which caused a reduction in the pressure on the upper surface. At the same time, the pressure on the lower surface increased when the anticlockwise vortex V_{ac1} disintegrated and broke down, propagated downstream, and moved away from the leading edge. Accordingly, the lift continued climbing while the pressure drag kept dropping until instant *ix* when the transient lift rose back to its maximum, whereas the pressure drag declined to its first minimum. It returned to a new periodic starting instant *i* of a new cycle.

The alternating propagation of vortices V_c and V_{ac} in UVS and LVS caused cyclic variations in the lift and drag coefficients. Compared to the vortex evolution and unsteady characteristics of the front wing solely taking place near the trailing edge, the complex vortex system and its evolution on the back wing significantly influenced the pressure fluctuations and distributions over the entire chord. The most prominent features on the back wing shown in Fig. 19 were the drastic pressure variations near the leading edge due to the migration of the high-pressure area influenced by the counter-rotating vortices from the upstream wake and the extra adverse pressure gradient zones on the suction side due to the induced secondary vortex. The upstream wake passageways on the back wing led to alternate strengthening and weakening of vortex-related pressure zones on both the upper and lower surfaces. It is conceivable that the intensified lift fluctuations were mainly attributed to the large-scale vortical wake from upstream constantly interfering with the back wing, which resulted in alternating pressure variations mainly in the vicinity of the leading edge. The upstream vortices and interactions resulted in the SVS traveling on the upper surface and shedding into the back-wing wake beyond the trailing edge in a turbulent state. The time-averaged net effects are credited to the wake-induced secondary vortices on the suction surface for providing the enlarged extra low-pressure zones resulting from the adverse pressure gradient on the upper surface of the back wing.

IV. Conclusions

The tandem stationary wing configuration at a low Reynolds number $Re = 10{,}000$ was investigated in terms of unsteady aerodynamic characteristics and interactions between the tandem wings using 3-D DNS. Two NACA 0012 wings at a low angle of attack $\alpha = 4$ deg were placed in line without a vertical offset. In this study, the state-of-the-art VI method of the Liutex vector was applied to capture the coherent structures in the flow, revealing the detailed

Table 3 Spanwise-averaged pressure coefficient on the upper/lower surface and lift coefficient for the back wing at nine typical instants

Instant	*i*	*ii*	*iii*	*iv*	*v*	*vi*	*vii*	*viii*	*ix*
C_p (upper)	−0.4238	−0.3991	−0.3252	−0.2327	−0.2106	−0.2155	−0.2533	−0.3364	−0.3800
C_p (lower)	−0.0343	−0.0724	−0.1425	−0.2033	−0.1996	−0.1332	−0.0785	−0.0024	0.0113
C_L	0.3895	0.3267	0.1828	0.0294	0.0110	0.0823	0.1747	0.3339	0.3912

vortical structures and improving the understanding of the aerodynamic advantages gained on the back wing.

The vortex shedding from the front wing gave rise to downstream disturbances in the form of wake vortex passages, significantly influencing the force variations and coherent structure evolution on the back wing. The UVS induced disturbances near the leading edge, giving rise to near-wall secondary vortices, which were found at an initial wavelength of $\lambda_z = 0.167$ in the spanwise direction. The secondary instability was rapidly amplified, causing the induced secondary vortices to evolve into 3-D Λ-shaped structures during the early transition. With intensive ejection and sweep effects, the Λ-shaped secondary vortices interacted with the UVS and merged into the hairpin-type vortices, leading to energy mixing and high-momentum stream injecting into the SVS near the boundary layer. The vortex interactions amplified the 3-D destabilization and affected the secondary instability downstream, where the spanwise wavelength of the vortices in the late transition was found to be approximately $\lambda_z = 0.125$, consistent with the spanwise fluctuations in the upstream wake. The downstream turbulent boundary layer was more tightly attached to the upper surface, which was beneficial for suppressing the flow separation downstream and allowing the vortices to travel smoothly across the trailing edge until they shed into the back-wing wake without forming noticeable recirculation zones like those on the front wing.

Because of the incoming wake, the induced secondary vortices inherited the baseline periodicity from the upstream wake interference. Some significant subharmonic frequencies multiple of the base frequency were found on the back wing, especially in the pressure drag signal, which was attributed to the nonlinear mutual interactions between the upstream vortex streets and the near-wall secondary vortices. These interactions accelerated the transition in the turbulent boundary layer and produced multiscale phenomena around the back wing.

The back wing gained significant aerodynamic benefits, as reflected by the enhanced lift and reduced drag. Comparisons of the time-averaged flowfields around the front and back wings revealed that the incoming vortices from the front wing energized the instability in the downstream boundary layer near the back wing, which presented an overall effect of suppressing the flow separation and thereby eliminating the large-scale vortical structures near the wing trailing edge. The detailed transient and coherent structure analyses suggest that the induced secondary vortices played a crucial role in the lift enhancement of the back wing by constantly generating vortex-related low-pressure zones on the suction wall surface, which is concluded as the mechanism behind the aerodynamic performance enhancement of the back wing. Moreover, the intensive fluctuations in the forces on the back wing largely contributed to the upstream wake passages passing through the back wing and altering the pressure variations on the leading edge.

Obviously, the aerodynamic advantages in the tandem wings due to the interactions between the incoming vortex streets and the induced secondary vortices were expected to strongly depend on the main parameters of the Reynolds number, angles of attack, and tandem location arrangement. Further investigations of tandem-wing configurations must be conducted using a matrix of these main parameters. This can provide an invaluable DNS database for the aerodynamics community to address the challenging problems of wing turbulence and their nonlinear aerodynamic interactions.

Acknowledgments

The authors acknowledge the financial funding support from the Shanghai Municipal Education Commission (grant number AR960) and Shanghai Municipal Science and Technology Commission (grant number 20 JC1413700).

References

[1] Zhang, Z., Wang, Z., and Gursul, I., "Lift Enhancement of a Stationary Wing in a Wake," *AIAA Journal*, Vol. 58, No. 11, 2020, pp. 4613–4619. https://doi.org/10.2514/1.J059872

[2] Rival, D., Manejev, R., and Tropea, C., "Measurement of Parallel Blade–Vortex Interaction at Low Reynolds Numbers," *Experiments in Fluids*, Vol. 49, No. 1, 2010, pp. 89–99. https://doi.org/10.1007/s00348-009-0796-1

[3] Olson, E. C., and Selberg, B., "Experimental Determination of Improved Aerodynamic Characteristics Utilizing Biplane Wing Configurations," *Journal of Aircraft*, Vol. 13, No. 4, 1976, pp. 256–261. https://doi.org/10.2514/3.44523

[4] Scharpf, D. F., and Mueller, T. J., "Experimental Study of a Low Reynolds Number Tandem Airfoil Configuration," *Journal of Aircraft*, Vol. 29, No. 2, 1992, pp. 231–236. https://doi.org/10.2514/3.46149

[5] Gong, W. Q., Jia, B. B., and Xi, G., "Experimental Study on Mean Thrust of Two Plunging Wings in Tandem," *AIAA Journal*, Vol. 53, No. 6, 2015, pp. 1693–1705. https://doi.org/10.2514/1.J053452

[6] Arranz, G., Flores, O., and Garcia-Villalba, M., "Three-Dimensional Effects on the Aerodynamic Performance of Flapping Wings in Tandem Configuration," *Journal of Fluids and Structures*, Vol. 94, April 2020, Paper 102893. https://doi.org/10.1016/j.jfluidstructs.2020.102893

[7] Zhu, Q., Wolfgang, M., Yue, D., and Triantafyllou, M., "Three-Dimensional Flow Structures and Vorticity Control in Fish-Like Swimming," *Journal of Fluid Mechanics*, Vol. 468, Oct. 2002, pp. 1–28. https://doi.org/10.1017/S002211200200143X

[8] Hemelrijk, C. K., and Hildenbrandt, H., "Schools of Fish and Flocks of Birds: Their Shape and Internal Structure by Self-Organization," *Interface Focus*, Vol. 2, No. 6, 2012, pp. 726–737. https://doi.org/10.1098/rsfs.2012.0025

[9] Broering, T. M., and Lian, Y.-S., "The Effect of Phase Angle and Wing Spacing on Tandem Flapping Wings," *Acta Mechanica Sinica*, Vol. 28, Dec. 2012, pp. 1557–1571. https://doi.org/10.1007/s10409-012-0210-8

[10] Moschetta, J.-M., and Thipyopas, C., "Aerodynamic Performance of a Biplane Micro Air Vehicle," *Journal of Aircraft*, Vol. 44, No. 1, 2007, pp. 291–299. https://doi.org/10.2514/1.23286

[11] Faure, T. M., Hétru, L., and Montagnier, O., "Aerodynamic Features of a Two-Airfoil Arrangement," *Experiments in Fluids*, Vol. 58, Sept. 2017, pp. 1–17. https://doi.org/10.1007/s00348-017-2429-4

[12] Faure, T. M., Dumas, L., and Montagnier, O., "Numerical Study of Two-Airfoil Arrangements by a Discrete Vortex Method," *Theoretical and Computational Fluid Dynamics*, Vol. 34, No. 1, 2020, pp. 79–103. https://doi.org/10.1007/s00162-019-00511-0

[13] Shah, S., and Ahmed, A., "On the Secondary Stall of a Wing in Tandem Configuration," *Aeronautical Journal*, Vol. 128, Feb. 2024, pp. 1–14. https://doi.org/10.1017/aer.2024.7

[14] Jones, R., Cleaver, D., and Gursul, I., "Aerodynamics of Biplane and Tandem Wings at Low Reynolds Numbers," *Experiments in Fluids*, Vol. 56, June 2015, Paper 124. https://doi.org/10.1007/s00348-015-1998-3

[15] Lefebvre, J. N., and Jones, A. R., "Experimental Investigation of Airfoil Performance in the Wake of a Circular Cylinder," *AIAA Journal*, Vol. 57, No. 7, 2019, pp. 2808–2818. https://doi.org/10.2514/1.J057468

[16] Rockwell, D., "Vortex-Body Interactions," *Annual Review of Fluid Mechanics*, Vol. 30, No. 1, 1998, pp. 199–229. https://doi.org/10.1146/annurev.fluid.30.1.199

[17] Gursul, I., and Rockwell, D., "Vortex Street Impinging Upon an Elliptical Leading Edge," *Journal of Fluid Mechanics*, Vol. 211, Feb. 1990, pp. 211–242. https://doi.org/10.1017/S0022112090001550

[18] Lua, K. B., Lu, H., Zhang, X., Lim, T., and Yeo, K., "Aerodynamics of Two-Dimensional Flapping Wings in Tandem Configuration," *Physics of Fluids*, Vol. 28, No. 12, 2016, Paper 121901. https://doi.org/10.1063/1.4971859

[19] Barnes, C. J., and Visbal, M. R., "Counterclockwise Vortical-Gust/Airfoil Interactions at a Transitional Reynolds Number," *AIAA Journal*, Vol. 56, No. 7, 2018, pp. 2540–2552. https://doi.org/10.2514/1.J056711

[20] Barnes, C. J., and Visbal, M. R., "Clockwise Vortical-Gust/Airfoil Interactions at a Transitional Reynolds Number," *AIAA Journal*, Vol. 56, No. 10, 2018, pp. 3863–3874. https://doi.org/10.2514/1.J057262

[21] Hayakawa, M., and Hussain, F., "Three-Dimensionality of Organized Structures in a Plane Turbulent Wake," *Journal of Fluid Mechanics*, Vol. 206, Sept. 1989, pp. 375–404. https://doi.org/10.1017/S0022112089002338

[22] Gupta, S., Zhao, J., Sharma, A., Agrawal, A., Hourigan, K., and Thompson, M. C., "Two- and Three-Dimensional Wake Transitions of a NACA0012 Airfoil," *Journal of Fluid Mechanics*, Vol. 954, Jan. 2023, Paper A26. https://doi.org/10.1017/jfm.2022.958

[23] Son, O., Gao, A.-K., Gursul, I., Cantwell, C. D., Wang, Z., and Sherwin, S. J., "Leading-Edge Vortex Dynamics on Plunging Airfoils and Wings," *Journal of Fluid Mechanics*, Vol. 940, June 2022, Paper A28. https://doi.org/10.1017/jfm.2022.224

[24] Li, Y., and Niu, X., "Rod–Airfoil Interaction Noise at Different Rod Cross Sections and Airfoil Angles," *AIAA Journal*, Vol. 60, No. 6, 2022, pp. 3635–3650. https://doi.org/10.2514/1.J061303

[25] Zhang, Z., Wang, Z., and Gursul, I., "Aerodynamics of a Wing in Turbulent Bluff Body Wakes," *Journal of Fluid Mechanics*, Vol. 937, April 2022, Paper A37. https://doi.org/10.1017/jfm.2022.132

[26] Huang, R., Wu, J., Jeng, J., and Chen, R., "Surface Flow and Vortex Shedding of an Impulsively Started Wing," *Journal of Fluid Mechanics*, Vol. 441, Aug. 2001, pp. 265–292. https://doi.org/10.1017/S002211200100489X

[27] Yarusevych, S., Sullivan, P. E., and Kawall, J. G., "On Vortex Shedding from an Airfoil in Low-Reynolds-Number Flows," *Journal of Fluid Mechanics*, Vol. 632, Aug. 2009, pp. 245–271. https://doi.org/10.1017/S0022112009007058

[28] Muyao Li, H. X., "Investigation of Aerodynamic Interactions Between NACA0012 Airfoils in Tandem," *32nd Congress of the International Council of the Aeronautical Sciences*, ICAS Paper 2020_1063, Sept. 2021.

[29] Hunt, J. C., Wray, A. A., and Moin, P., "Eddies, Streams, and Convergence Zones in Turbulent Flows," *Proceedings of the 1988 Summer Program*, Center for Turbulence Research, Stanford, CA, 1988, pp. 193–208.

[30] Chong, M. S., Perry, A. E., and Cantwell, B. J., "A General Classification of Three-Dimensional Flow Fields," *Physics of Fluids A: Fluid Dynamics*, Vol. 2, No. 5, 1990, pp. 765–777. https://doi.org/10.1063/1.857730

[31] Zhou, J., Adrian, R. J., Balachandar, S., and Kendall, T., "Mechanisms for Generating Coherent Packets of Hairpin Vortices in Channel Flow," *Journal of Fluid Mechanics*, Vol. 387, May 1999, pp. 353–396. https://doi.org/10.1017/S002211209900467X

[32] Jeong, J., and Hussain, F., "On the Identification of a Vortex," *Journal of Fluid Mechanics*, Vol. 285, Feb. 1995, pp. 69–94. https://doi.org/10.1017/S0022112095000462

[33] Liu, C., Gao, Y., Tian, S., and Dong, X., "Rortex—A New Vortex Vector Definition and Vorticity Tensor and Vector Decompositions," *Physics of Fluids*, Vol. 30, No. 3, 2018, Paper 035103. https://doi.org/10.1063/1.5023001

[34] Gao, Y., and Liu, C., "Rortex and Comparison with Eigenvalue-Based Vortex Identification Criteria," *Physics of Fluids*, Vol. 30, No. 8, 2018, Paper 085107. https://doi.org/10.1063/1.5040112

[35] Xu, H., "Direct Numerical Simulation of Turbulence in a Square Annular Duct," *Journal of Fluid Mechanics*, Vol. 621, Feb. 2009, pp. 23–57. https://doi.org/10.1017/S0022112008004813

[36] Wang, D., Liu, Y., Li, H., and Xu, H., "Secondary Instability of Channel-Confined Transition Around Dual-Circular Cylinders in Tandem," *International Journal of Mechanical Sciences*, Vol. 208, Oct. 2021, Paper 106692. https://doi.org/10.1016/j.ijmecsci.2021.106692

[37] Kim, J., and Moin, P., "Application of a Fractional-Step Method to Incompressible Navier-Stokes Equations," *Journal of Computational Physics*, Vol. 59, No. 2, 1985, pp. 308–323. https://doi.org/10.1016/0021-9991(85)90148-2

[38] Luo, K., Zhuang, Z., Fan, J., and Haugen, N. E. L., "A Ghost-Cell Immersed Boundary Method for Simulations of Heat Transfer in Compressible Flows Under Different Boundary Conditions," *International Journal of Heat and Mass Transfer*, Vol. 92, Jan. 2016, pp. 708–717. https://doi.org/10.1016/j.ijheatmasstransfer.2015.09.024

[39] Luo, K., Luo, Y., Jin, T., and Fan, J., "Studies on Shock Interactions with Moving Cylinders Using Immersed Boundary Method," *Physical Review Fluids*, Vol. 2, No. 6, 2017, Paper 064302. https://doi.org/10.1103/PhysRevFluids.2.064302

[40] Zhang, W., and Samtaney, R., "Assessment of Spanwise Domain Size Effect on the Transitional Flow Past an Airfoil," *Computers & Fluids*, Vol. 124, Jan. 2016, pp. 39–53. https://doi.org/10.1016/j.compfluid.2015.10.008

[41] Moin, P., and Mahesh, K., "Direct Numerical Simulation: A Tool in Turbulence Research," *Annual Review of Fluid Mechanics*, Vol. 30, No. 1, 1998, pp. 539–578. https://doi.org/10.1146/annurev.fluid.30.1.539

[42] Lee, D., Nonomura, T., Oyama, A., and Fujii, K., "Comparison of Numerical Methods Evaluating Airfoil Aerodynamic Characteristics at Low Reynolds Number," *Journal of Aircraft*, Vol. 52, No. 1, 2015, pp. 296–306. https://doi.org/10.2514/1.C032721

[43] Yuta, Y., Tomohisa, O., and Akinori, M., "1201 Pressure Distribution on a NACA0012 Airfoil at Low Reynolds Numbers," *Proceedings of the International Conference on Jets, Wakes and Separated Flows (ICJWSF) 2013.4*, Japan Soc. of Mechanical Engineers, Tokyo, Japan, 2013, pp. 1201-1–1201-5. https://doi.org/10.1299/jsmeicjwsf.2013.4._1201-1_

[44] Winslow, J., Otsuka, H., Govindarajan, B., and Chopra, I., "Basic Understanding of Airfoil Characteristics at Low Reynolds Numbers ($10^4 - 10^5$)," *Journal of Aircraft*, Vol. 55, No. 3, 2018, pp. 1050–1061. https://doi.org/10.2514/1.C034415

[45] Bokaian, A., and Geoola, F., "Wake Displacement as Cause of Lift Force on Cylinder Pair," *Journal of Engineering Mechanics*, Vol. 111, No. 1, 1985, pp. 92–99. https://doi.org/10.1061/(ASCE)0733-9399(1985)111:1(92)

[46] Wang, Z., and Gursul, I., "Lift Enhancement of a Flat-Plate Airfoil by Steady Suction," *AIAA Journal*, Vol. 55, No. 4, 2017, pp. 1355–1372. https://doi.org/10.2514/1.J055382

[47] Balakumar, P., "Direct Numerical Simulation of Flows over an NACA-0012 Airfoil at Low and Moderate Reynolds Numbers," *47th AIAA Fluid Dynamics Conference*, AIAA Paper 2017-3978, June 2017. https://doi.org/10.2514/6.2017-3978

[48] Anyoji, M., Nonomura, T., Aono, H., Oyama, A., Fujii, K., Nagai, H., and Asai, K., "Computational and Experimental Analysis of a High-Performance Airfoil Under Low-Reynolds-Number Flow Condition," *Journal of Aircraft*, Vol. 51, No. 6, 2014, pp. 1864–1872. https://doi.org/10.2514/1.C032553

[49] Tank, J., Klose, B., Jacobs, G., and Spedding, G., "Flow Transitions on a Cambered Airfoil at Moderate Reynolds Number," *Physics of Fluids*, Vol. 33, No. 9, 2021, Paper 093105. https://doi.org/10.1063/5.0061939

[50] Yarusevych, S., Kawall, J. G., and Sullivan, P. E., "Airfoil Performance at Low Reynolds Numbers in the Presence of Periodic Disturbances," *Journal of Fluids Engineering*, Vol. 128, No. 3, 2005, pp. 587–595. https://doi.org/10.1115/1.2175165

[51] Jones, L., Sandberg, R., and Sandham, N., "Direct Numerical Simulations of Forced and Unforced Separation Bubbles on an Airfoil at Incidence," *Journal of Fluid Mechanics*, Vol. 602, May 2008, pp. 175–207. https://doi.org/10.1017/S0022112008000864

[52] Huang, R. F., and Lin, C. L., "Vortex Shedding and Shear-Layer Instability of Wing at Low-Reynolds Numbers," *AIAA Journal*, Vol. 33, No. 8, 1995, pp. 1398–1403. https://doi.org/10.2514/3.12561

[53] Wang, J., Wang, J., and Kim, K. C., "Wake/Shear Layer Interaction for Low-Reynolds-Number Flow over Multi-Element Airfoil," *Experiments in Fluids*, Vol. 60, No. 1, 2019, pp. 1–24. https://doi.org/10.1007/s00348-018-2662-5

[54] Wang, Y.-Q., Gao, Y.-S., Liu, J.-M., and Liu, C., "Explicit Formula for the Liutex Vector and Physical Meaning of Vorticity Based on the Liutex-Shear Decomposition," *Journal of Hydrodynamics*, Vol. 31, April 2019, pp. 464–474. https://doi.org/10.1007/s42241-019-0032-2

[55] Xu, H., Cai, X.-S., and Liu, C., "Liutex (Vortex) Core Definition and Automatic Identification for Turbulence Vortex Structures," *Journal of Hydrodynamics*, Vol. 31, Aug. 2019, pp. 857–863. https://doi.org/10.1007/s42241-019-0066-5

[56] Mandal, A., and Dey, J., "An Experimental Study of Boundary Layer Transition Induced by a Cylinder Wake," *Journal of Fluid Mechanics*, Vol. 684, Oct. 2011, pp. 60–84. https://doi.org/10.1017/jfm.2011.270

[57] Weihs, D., and Katz, J., "Cellular Patterns in Poststall Flow over Unswept Wings," *AIAA Journal*, Vol. 21, No. 12, 1983, pp. 1757–1759. https://doi.org/10.2514/3.8321

[58] Pan, C., Wang, J. J., Zhang, P. F., and Feng, L. H., "Coherent Structures in Bypass Transition Induced by a Cylinder Wake," *Journal of Fluid Mechanics*, Vol. 603, May 2008, pp. 367–389. https://doi.org/10.1017/S0022112008001018

[59] Wang, J.-S., and Wang, J.-J., "Wake-Induced Transition in the Low-Reynolds-Number Flow over a Multi-Element Airfoil," *Journal of Fluid Mechanics*, Vol. 915, May 2021, Paper A28. https://doi.org/10.1017/jfm.2021.20

[60] Wang, J.-S., Wu, J., and Wang, J.-J., "Wake-Triggered Secondary Vortices over a Cylinder/Airfoil Configuration," *Experiments in Fluids*, Vol. 64, No. 1, 2023, p. 6. https://doi.org/10.1007/s00348-022-03546-y

[61] Marxen, O., Lang, M., and Rist, U., "Vortex Formation and Vortex Breakup in a Laminar Separation Bubble," *Journal of Fluid Mechanics*, Vol. 728, Aug. 2013, pp. 58–90. https://doi.org/10.1017/jfm.2013.222

[62] Kirk, T. M., and Yarusevych, S., "Vortex Shedding Within Laminar Separation Bubbles Forming over an Airfoil," *Experiments in Fluids*, Vol. 58, April 2017, pp. 1–17. https://doi.org/10.1007/s00348-017-2308-z

[63] He, G.-S., Pan, C., Feng, L.-H., Gao, Q., and Wang, J.-J., "Evolution of Lagrangian Coherent Structures in a Cylinder-Wake Disturbed Flat Plate Boundary Layer," *Journal of Fluid Mechanics*, Vol. 792, April 2016, pp. 274–306. https://doi.org/10.1017/jfm.2016.81

[64] Huang, R., and Wu, J., "Effects of Cylinder Wake on Separated Boundary Layer of a Wing," *AIAA Journal*, Vol. 45, No. 1, 2007, pp. 247–256. https://doi.org/10.2514/1.24517

I. Gursul
Associate Editor